2015

Colloidal Synthesis and Optical Characterizations of Semiconductor Nanocrystals from Nontoxic Elements

Minh Q. Ho
Virginia Commonwealth University

COLLOIDAL SYNTHESIS AND OPTICAL CHARACTERIZATIONS OF SEMICONDUCTOR NANOCRYSTALS FROM NONTOXIC ELEMENTS

By Minh Q. Ho, M.S.

A thesis submitted in partial fulfillment of the requirements for the degree of Master of Science in Chemistry at Virginia Commonwealth University.

Virginia Commonwealth University, 2015.

Advisor: Indika U. ArachchigeAssistant Professor, Department of Chemistry.

TABLES OF CONTENTS

ACKNOWLEDGEMENT

To start thinking about all the great people who have helped me along the way towards my degree, I would have to go first with my precious family, my mother, father and little sister. Without them, I would not literally be here or anywhere in life. As an international student who has stayed by himself to study in the US for the last eleven years, the frequent communication with my parents have kept me in check mentally, and motivated me to move forward to complete my journey in graduate school. For the distance between my hometown and the States, they would have not able to directly help me anything physically, but their continuous love and encouragement was enough for me to be grateful every single day. I could remember having my mother involved in all of my big decisions such as choosing colleges, changing majors and picking schools, it was just like having my best friend walking with me throughout my entire education. For many foreign students living abroad, most of them tell me the longest conversation with their parents can last up to 15 minutes. In my case, I cannot keep my phone down when talking to my mother and our conversation could go for hours. There were so many things that she and I could discuss about regarding family, my studies and all other aspects of my life. I can proudly say that she was my closest friend and the best life mentor through all these years. My father is a man with less word, so our father-and-son talks were quite brief most of the time, and my mother always had to ask him whether he wanted to talk to me. I know he loved me very much but I am probably lousy in keeping his interest when talking to me. He has devoted his entire heart and mind to

my little sister who has been sick since she was born, and I am always grateful for that. Because of her, he has given up so many opportunities so that he can always be there when she needs anything. I am so blessed to have such a happy and supportive family (gia dinh) back home; they have been my mental backbone and I can do anything knowing they will always have my back.

The next most important person I would like to thank is my research advisor Dr. Indika U. Arachchige. Being a young professor, his activeness and sincerity in the research lab kept me moving towards my goals, for I am often distracted by many activities in college community. I could remember him keeping us on track through all of our presentations, groups meetings, literature seminars, proposals and so on. As graduate students, we often have a tendency to procrastinate things till the last moment, especially me, and he has straightened me out with his consistent reminders and revisions. I sometimes do feel stressed and frustrated, but deep down I understand that it is absolutely necessary for my growth towards my degree and future professional career. I could remember like it was yesterday when he went through so much difficulties and frustrations during a project of mine. I made so many mistakes and caused him lots of troubles, yet he was always patient to help me out to complete what was necessary. I guess it is a privilege to have an advisor who always spends time mentoring us in every aspect in the laboratory, though I must admit sometimes I felt it was too much.

I would also like to give my sincere appreciation to Dr. Michael Hunnicutt, my professor in Instrumental Analysis laboratory, where I performed my teaching assistantship for the last 5 years. With lots of experiences from many years in the

industry, he taught me so much about how to properly teach and help students understand the concepts and applications of the performed experiments. He showed me how to adjust a difficult and lengthy experiment so that it would be challenging enough, yet the students can have enough time to be fully comfortable with the instruments. Most students taking this course are on either senior or graduate level, so being familiar with the instrumentations is a crucial step for them to step into their professional careers or graduate studies. Moreover, there are lots of professional attributes that I could learn from Dr. Hunnicutt that they could help me tremendously in my future career.

Finally, I would like to thank all of my colleagues in Dr. Arachchige lab for all their helps in my lab work. Among them, Richard J Esteves, who is the co-author of my final project, has helped me tremendously in some of the important data analysis and writing of my last paper. Lamia Nahar and Xiaonan Gao have always been there to help me with some of my lab work and seminar preparations. Although he is the newest member in our group, Venkatesh Tallapally has developed a great friendship with me and is always willing to give me a hand in anything. Our group had the privilege to have two postdoc working with us, Dr. Gotluru Kedarnath and Dr. Kulugammana Ranmohotti, and they were great assets to our group and have mentored me a lot as well. Last but not least is my great friend Dr. Khaled AbouZeid, who have helped me through many things inside as well as outside of the laboratory and I am very thankful for that. All of these great people are the ones who have helped me shaping up who I am today as a scientist and I will never forget what I have learned from them.

LIST OF FIGURES

LIST OF TABLES

Abstract

COLLOIDAL SYNTHESIS AND OPTICAL CHARACTERIZATIONS OF
SEMICONDUCTOR NANOCRYSTALS FROM NONTOXIC ELEMENTS

By Minh Q. Ho, M.S.

To date, the search efforts have shifted from the toxic II-VI, III-V and IV-VI semiconductors to more environmentally friendly materials. Among Group II-V semiconductors, Zn_3P_2 has shown to be a more benign option, similar to Group IV (Ge, Si) materials, for future applications in photovoltaics and optoelectronics. This work is dedicated to the development of wet-chemical synthetic routes of (1) Zn_3P_2 and (2) Group IV (Ge, Si, $Si_{1-x}Ge_x$) nanocrystals with precise control over composition, crystal structure, size and dispersity by adjusting different reaction parameters such as temperature, time and solvent composition. Different characterizations will also be

employed to probe the size- and composition-dependent physical and optical properties of resulting products.

The first part of this work illustrates the synthesis of luminescent Zn_3P_2 nanocrystals, an earth-abundant and a direct-gap semiconductor possessing high absorption coefficient and long carrier diffusion length, which uphold promising potential in many optoelectronic applications. A hot injection method by using highly reactive P and Zn precursors ($P[Si(CH_3)_3]_3$ and diethyl zinc) in hexadecylamine and octadecene was developed to prepare a series of alkyl-amine-passivated tetragonal Zn_3P_2 crystallites with varying size sizes. Substantial blue shifts in the absorption onsets (2.11−2.73 eV) in comparison to the bulk counterpart (1.4−1.5 eV) and a clear red shift with increasing particle size indicates the quantum confinement effects. This is also consistent with the photoluminescent studies with the size-tunable maxima in the visible region (469−545 nm) as a function of growth temperature and time. The phase purity and alkyl-amine passivation of the nanocrystals were determined by structural and surface analysis, confirming the presence of N–Zn and N–P bonds on the tetragonal Zn_3P_2 crystallites.

The second part of this works focuses on the development of a colloidal synthetic strategy of alkyl-amine capped $Si_{1-x}Ge_x$ nanocrystals with control over size- and composition-dependent optical properties. Despite their high miscibility at all compositions, developing a wet-chemical synthesis of $Si_{1-x}Ge_x$ alloys in the nanoscale remains a challenging task, owing to the difference of their crystallization temperatures and the high surface oxidation of Si. Thus an adapted colloidal method is utilized to fabricate single-element Ge and Si nanocrystals. Powder X-ray diffraction indicates successful production of cubic crystalline Ge and amorphous Si nanoparticles

individually in oleylamine/octadecene (surfactant/solvent) mixture at 300°C. Absorption onset values of 1.28 eV and 3.11 eV are obtained for resulting Ge and Si colloids, respectively. By alloying these two materials in their nano-regime, tunable optical properties can be achieved throughout the visible to the near IR region by simply varying their elemental compositions. The success of this bandgap engineering process offers more options for new material design by taking advantage of unique properties from each component material.

CHAPTER 1

INTRODUCTION

Materials with at least one of its dimensions approaching the length scale of 1–100 nm are commonly referred to as nanomaterials, which exhibit many fundamental properties different from their bulk solid systems.[1-3] Research in nanotechnology has been expanded across multiple disciplines of science and has given rise to various potential applications in electronics, optoelectronics, catalysis, and energy conversion. These potentials have led to substantial research efforts in exploring new synthetic methodologies and unique properties of different nanomaterials. Since several fabrication methods have been developed over the years, it is important to identify the one that produces the highest quality with acceptable yield of product so that it is more suitable for real life applications. Since most of the well-studied fluorescent semiconductor quantum dots are composed of toxic elements (Cd, As, Se, Pb), which are detrimental to the environment and living cells, and health concerns have prohibited the wider their uses in biological applications, the task to look for more benign alternatives has become a focus in this field of nanotechnology. This thesis is focused on the synthetic development of low- to non-toxic semiconductor nanocrystals (NCs) from group II-V and IV elements, and tuning of different synthetic conditions to achieve products with the desired structures and properties. This chapter is dedicated to describe the importance of nanotechnology, the quantum size effects in semiconductor nanoparticles (NPs) that are not observed in their bulk counterparts, different synthetic

approaches reported and why we are interested in developing colloidal synthesis of Zn_3P_2 and Group IV NPs.

1.1. Nanomaterials

The first reported syntheses of nanomaterials began as early as 1857 when Michael Faraday produced the aqueous solution of Au NPs.[4] However, most following efforts were only focused on the larger sizes (>100 nm), where little to no changes occur in their properties as a function of size. In the last few decades, materials in the size range of 1–100 nm have drawn intensive research interest owing to their unique changes in fundamental properties that are not present in the macroscale. In general, material size can range from the scale where it does not matter how big it is to one where it cannot be divided anymore, and nanoscience is the study of matter in that intermediate regime, where every slight modification in sizes can lead to several changes in its fundamental properties. These unique changes in material properties are the scope of many scientific investigations in order to probe new capabilities of materials that are useful in technology, medicine and general uses. However, commercial manufactures of nanomaterials today are still limited because the high production cost still outweighs their improvements of properties. Thus most research efforts are directed towards specific novel properties that are demanded and not attainable in the bulk.

Once a material physical size falls into the nano-regime, one of the most important changes is the significant increase in surface area with respect to its volume. The overall number of atoms in a crystal structure unit decreases dramatically, and surface atoms become more important to several intrinsic properties such as magnetic,[5,6]

optoelectronic[7,8] and catalytic.[9,10] In addition, further uses of nanomaterials have gone into the development of nanotechnology, which involve for miniaturization of functional devices. To date, production and engineering of materials in the nanoscale have grown tremendously in increasing number of structural and functional devices, both organic and inorganic, along with the investigation of their size-dependent mechanical, catalytic, optical, magnetic, electronic and electric properties.

Depending on the desired application, nanomaterials can be categorized into metals, semiconductors and magnets that can be in crystalline or amorphous form. For nanostructures composed of transition metals (Co, Ni),[11,12] bimetallic (CoPt, FePt),[13,14] metal pnictides (MnP, FeP)[15,16] and metal oxides (FeO, CuO, NiO),[17] rigorous studies have been done on their synthesis and characterization of their magnetic properties, which have been used in motors, inks and biomedical application. Magnetic Fe_2O_3 and Ni nanostructures have also been proven efficient in targeted drug delivery and bio-labeling for cancer therapy.[18,19] In catalysis industry, nanomaterials have been shown enhanced capability in catalyzing a variety of reactions including hydrogenation (Rh, Pt, Pd),[20,21] hydrodesulfurization (Ni_2P),[22] and hydrodenitrogenation (MoS_2).[23] In optoelectronics, a majority of studies have been performed on semiconductor nanostructures due to their drastic change in optical properties relative to that of the bulk material. This unique phenomenon has received a great deal of attention from the scientific community, making semiconductors the most studied type of nanomaterials.

1.2. Semiconductors

Semiconductors, by definition, belong to a group of material that displays an intermediate conductivity between conductors and insulators (Figure 1.1). On the macroscopic scale, a semiconductor is composed of a large network of ordered atoms that form a set of similar-energy molecular orbitals, resulting in the formation of a continuous band.[24] At 0 K, all electrons are occupied in the lower energy level (valence band, VB), leaving the higher energy level (conduction band, CB) empty. One characteristic feature of a semiconductor is the energy difference between the VB and CB, bandgap (E_g), and its magnitude is normally in the range of 0.3–3.8 eV[24] (Table 1.1) and distinct for each specific material. This band energy concept in semiconductors can be understood similarly to the molecular orbital theory for an individual molecule, thus E_g can also be defined as the minimum energy required to excite an electron from HOMO to LUMO. The difference in conductivity between insulators, semiconductors and conductors is illustrated in the difference of E_g value (Figure 1.1). The larger the bandgap energy, the harder it is for electrons to travel from VB to CB, resulting lower probability for electrons to conduct.

When absorbing photon energy that exceeds the energy gap, an electron in the VB can overcome the bandgap barrier and travel up to the CB,[24] leaving a positive hole in the VB. The electron and hole are mobilized and act as charge carriers with applied voltage; otherwise they exist as an electrostatically bound electron-hole pair (exciton) in their lowest energy state.[25] These characteristic excitons possess a finite size in the crystal structure, known as the Bohr radius (a_B), with its value estimation illustrated in eq 1.1

$$a_B \;=\; \frac{\hbar^2 \in}{e^2} \left[\frac{1}{m_e^*} + \frac{1}{m_h^*} \right] \tag{1.1}$$

where $\in$ is the dielectric coefficient, e is the elementary charge, m_e^* and m_h^* are electron and hole effective masses, respectively. Since $\in$, m_e^* and m_h^* are specific for each material, a_B can span a wide range of 1–100 nm.[25] The difference in many optoelectronic properties of semiconductors depends heavily on the comparability of the crystallite size and the Bohr radius. When crystallite size is equal or less than that of the Bohr radius, materials exhibit size-dependent absorption and emission properties, which have been a hot topic for many scientific investigations.
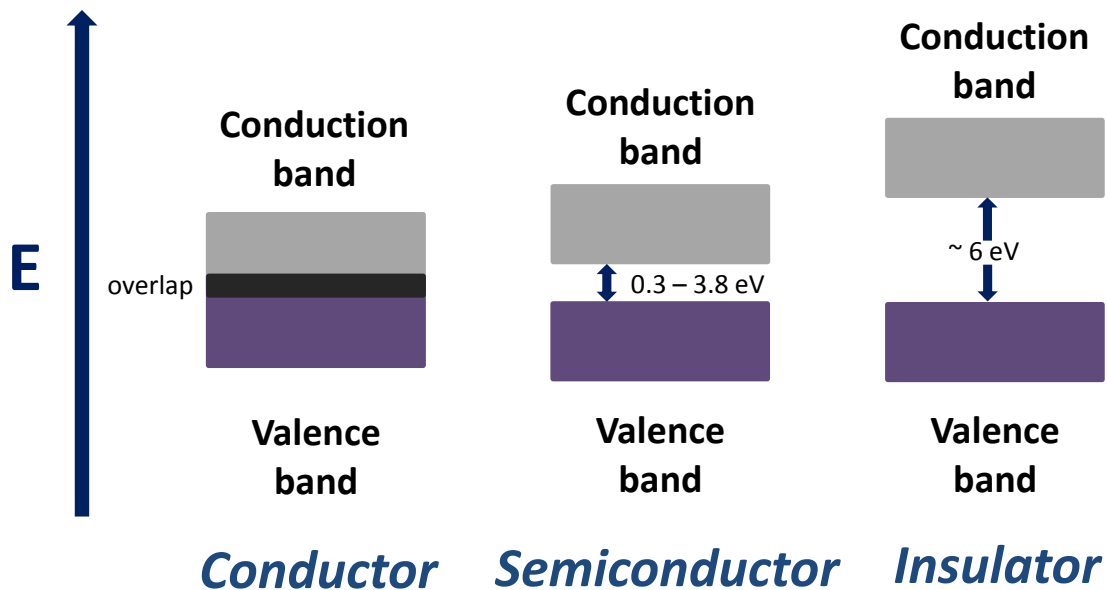
Figure 1.1. The energy gap difference between a conductor, semiconductor and an insulator.

Table 1.1. Properties and Applications of Semiconductors

Compound	Bandgap (eV)	Type*	Structure	Lattice spacing (Å)	Applications
Group III–V					
GaP	2.25	i	zinc blend	5.45	LEDs
GaAs	1.43	d	zinc blend	5.653	integrated circuits, displays
GaSb	0.69	d		6.095	thermal imaging devices
InP	1.28	d	zinc blend	5.8687	transistors
InAs	0.36	d	zinc blend	6.058	
InSb	0.17	d		6.4787	
Group II–VI					
CdS	2.53	d	wurtzite	4.136	photovoltaic cells
CdSe	1.74	d	wurtzite	4.299	photovoltaic cells
CdTe	1.5	d	zinc blend	6.477	photovoltaic cells, modulators
ZnS	3.8	d	wurtzite	3.814	phosphors, infrared windows
ZnSe	2.58	d	zinc blend	5.667	infrared windows, LEDs
ZnTe	2.28	d	zinc blend	6.101	
Group IV–VI					
PbS	0.37	d	sodium chloride	5.936	infrared sensors
PbSe	0.26	d	sodium chloride	6.124	infrared sensors
PbTe	0.29	d	sodium chloride	6.460	infrared sensors
Group IV					
Si	1.11	i	diamond	5.43	integrated circuits
Ge	0.67	i	diamond	5.66	power electronics

i. indirect gap; d. direct gap

When considering optical properties of semiconductors, they can be classified as either direct- or indirect-gap (Figure 1.2). All photon induced electronic transitions rely not only on the intensity of incident photon energy relative to E_g, but also the wave vector k. In direct-gap materials, the wave vectors of electrons are conserved during excitation to relaxation processes. The absorption coefficient is proportional to the probability of the electronic transition,[24] thus direct-gap semiconductors exhibit sharp absorption peaks with large absorption coefficients (e.g., CdSe, PbSe). Following the k-conserved excitation is the electron relaxation or the recombination of electron-hole pairs, which will emit energy in form of photons. This process is commonly known as radiative recombination photoluminescence. These processes are useful features of semiconductors since they can be used in light emitting diodes and laser applications. In contrast with direct-gap, the VB maximum and CB minimum of indirect-gap materials do not have the same wave vector k, resulting in forbidden electronic transitions due to non-conserving momentum condition[26] (e.g., Si, Ge). Electronic transitions are still able to occur for indirect band structure by the presence or removal of phonons (lattice vibrations) (Figure 1.2).[26] Nonetheless, phonon-induced transitions are rare phenomena, thus probability of exciton radiative recombination is much lower in indirect gap materials, reducing the absorption and emission efficiency. This limitation prohibits the use of indirect gap semiconductors (Si, Ge) in many optical and optoelectronic applications. In addition, non-radiative recombination of electron-hole pairs may also be caused by surface defects, impurities or dangling bonds that act as trapping states within the bandgap.[24] These mid-gap states serve as non-radiative sites that can

capture the photogenerated electrons and holes, prohibiting the possibility of band-edge recombination (Figure 1.3).

Direct bandgap   **Indirect bandgap**
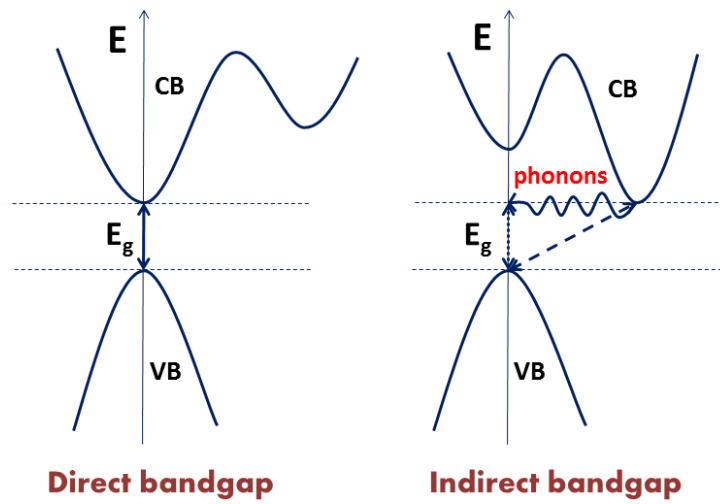
Figure 1.2. The difference in bandgap structure of a direct- and indirect–gap semiconductor.
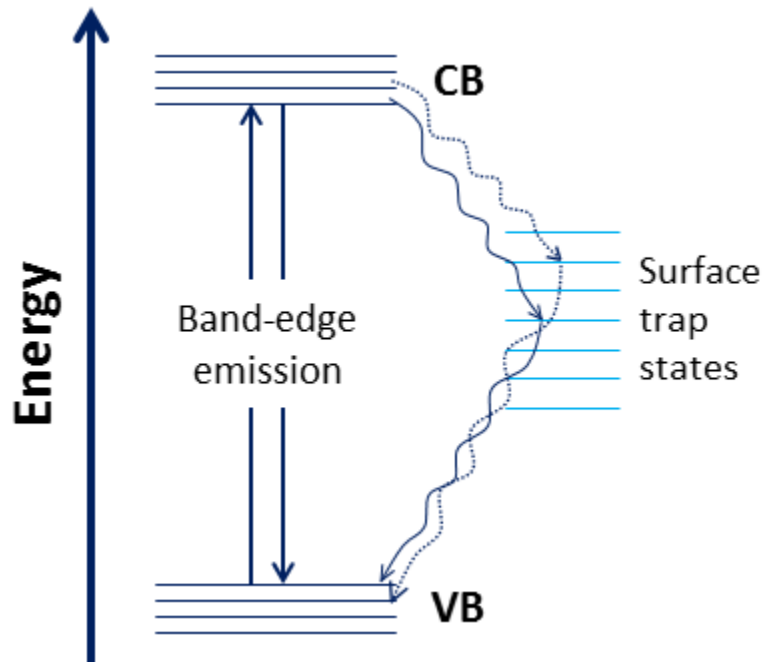
Figure 1.3. Representative energy diagram of semiconductor nanoparticles; straight and wavy arrows indicate band-edge and surface trap state emission, respectively.

1.3.   Semiconductor Nanoparticles

In the last two decades, the enormous changes in fundamental properties of semiconductor materials, whose sizes approach the nanoscale, have been the most studied research topic in nanotechnology. Among them, the most remarkable property of semiconductor NPs is the unusually large change in their optical properties as a function of size, allowing opportunities to exploit new photophysical properties of materials. For example, the bandgap of CdS can be tuned from 2.5 to 4.5 eV as the size of the bulk material are reduced to the molecular regime.[27] The melting temperature increases from 400 to 1600 °C[28] and pressure required for structural transformation varies of 9 to 2 GPa.[29]

When the size of a semiconductor material becomes comparable or smaller than the Bohr radius, bound physical space of the excitons become smaller, and they are considered to undergo the quantum confinement effect. When this happens, electrons and holes become much closer to each other, resulting in higher Coulombic interaction and kinetic energy due to increase in collisions.[30] In addition, all the similar energy levels forming the continuous band in the bulk are compressed to single discrete ones by the confinement effect.[31] This results in the splitting of VB and CB electronic bands into discrete energy levels, and a blue shift of E_g energy with respect to the bulk is observed as the particle size decreases (Figure 1.4). This inversely proportional relationship between the bandgap energy change (ΔE) and the particle size under quantum confinement effect can be explained by equation 1.2.[24]

$$\Delta E = \frac{\hbar^2 \pi^2}{2R^2} \left[\frac{1}{m_e^*} + \frac{1}{m_h^*} \right] - \frac{1.8e^2}{\epsilon R} \qquad (1.2)$$
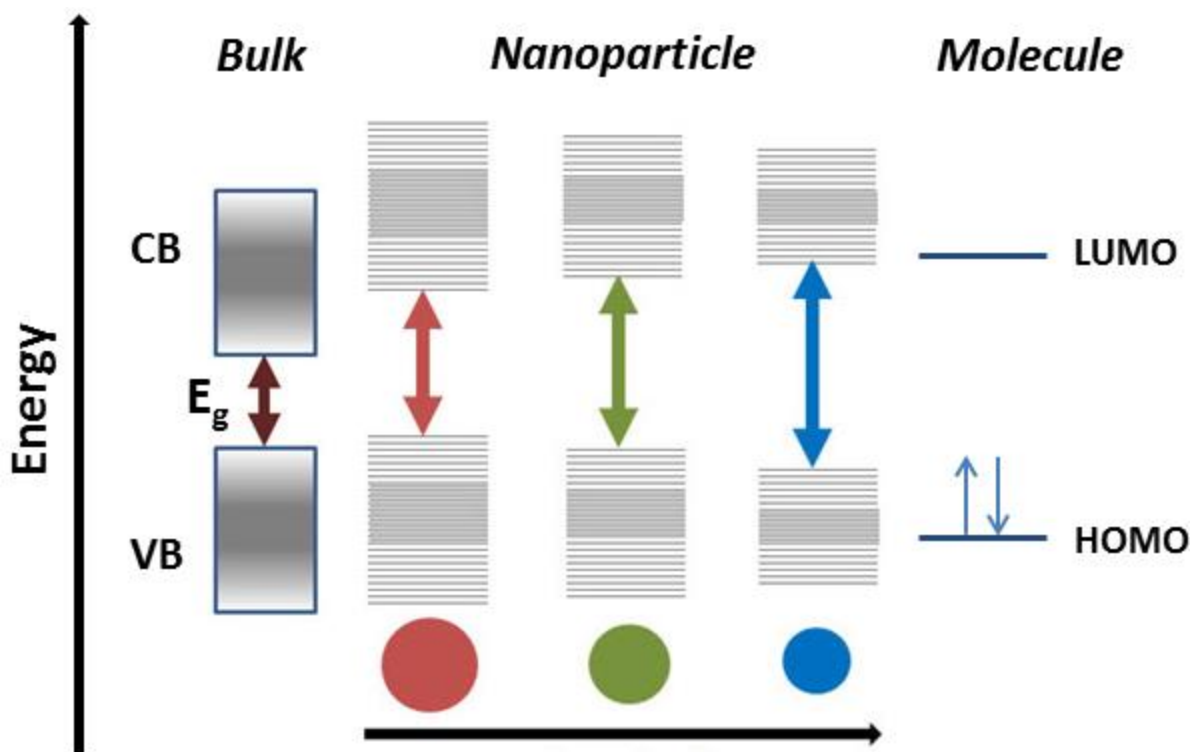
Figure 1.4. Continuous energy bands in bulk and discrete energy levels in nanoparticulate semiconductors with respect to molecular orbital theory for a single molecule.

Although this equation 1.2 is still an incomplete validation model to quantitatively correlate between calculated and experimental values due to a few presumptions of charge carrier effective mass and dielectric constant values, it gives a good estimation of the change in E_g as a function of particle size and clearly demonstrates size confinement effects in semiconductor NPs. Owing to this unique property, absorption and emission of semiconducting NPs can be fine-tuned by changing the particle size in the range of the critical radii, below which quantum confinement is observed. These values are highly dependent on the material and can range from 2.2 to 50 nm for group II-VI, IV-VI and III-V semiconductors.[24] This strong size-dependent feature is particularly

helpful in tuning the absorption and emission energy across a wide range of the electromagnetic spectrum. That is the reason semiconductor NPs have gained significant interest as promising candidates for solar cells,[32] nonlinear optical devices,[33] light emitting diodes,[34] and fluorescent bio-labelling.[35]

As mentioned above, the second most pronounced change in the semiconductor NPs is the enhanced surface/volume ratio, which also plays an important role in their optical properties. Since emission properties of NPs are contributed by both core and surface molecules, this surface enlargement can affect the dynamics of electron-hole recombinations. Compared to the bulk, more molecules in NPs are exposed on the surface, resulting in higher degree of defects and dangling bonds. These surface defects collectively form a series of mid-gap intermediate energy levels between the VB and CB, leading to the trapping photoexcited electrons or holes (Figure 1.3).[36] While band-edge absorption and emission are intrinsic in semiconductor NPs and exhibit sharp emission peaks, these trap-state energy levels reduce the probability of the band-edge transitions and exhibit much broader emission spectra in the longer wavelength. This surface effect has been shown to greatly reduce the quantum yield reduction in many luminescent NPs. Effective capping of the NP surface can greatly reduce this phenomenon, thus different surfactants have been used as a means for surface passivation and elimination of surface trap states.[36]

1.4.   Synthesis of Semiconductor Nanoparticles

To date, several synthetic routes have been developed and employed in the fabrication semiconductor NPs, and they are categorized into two types of top-down and

bottom-up techniques. In order to be used in any application, all prepared NPs will eventually be assembled in an orderly fashion into functional devices, hence it is crucial that these superstructures must be able to retain the novel properties of the building block particles. Thus development of a synthetic method requires high control of particle monodispersity along with structural and compositional purity. Although precise control of these properties still faces some challenges today, numerous routes have been established along with intensive investigation in the nucleation and growth mechanisms of different types of semiconductor NPs.

1.4.1. Top-Down techniques

In these techniques, a macroscale bulk semiconductor is etched down to form NPs by electron or ion beams. Controlled size and morphologies are achievable for this method due to high degree of flexibility in design and physical manipulation of the NPs by the high energy beam, allowing for systematic investigations of the quantum confinement effect for various particle sizes and shapes. One of the earliest examples of a top-down approach is reactive ion etching, which was employed for the fabrication of ZnTe quantum dot arrays using CH_4 and H_2.[37] In this process, a radio frequency induced plasma breaks down the gas molecules into reactive species, which are allowed to react with the sample surface to form volatile species and finally evaporate. Other techniques include focused ion beam and electron beam lithography, which were also used for preparation for nanostructures, yet these methods are rather slow with low reaction yield and require highly specialized equipment, making it less suitable for mass production. Due to these practical disadvantages, there have been much more efforts

12

spent on bottom-up methods since they offer low cost approaches with large production yield, high control of monodispersity and phase purity for resulting NP products.

1.4.2. Bottom-up techniques

Compared to the top-down approach, bottom-up technique has proven to be a more favorable method to fabricate semiconductor NPs, thus a number of methods, which are generally divided into vapor-phase and liquid-phase, have been developed.

1.4.2.1. Vapor-phase

This method utilizes the chemical supersaturation of vapor mixture, resulting in homogeneous nucleation of the gas molecules when the degree of supersaturation and condensation kinetics allow.[38] Upon formation of the nuclei, particle growth is facilitated by further deposition of supersaturated molecules onto the initial nuclei to form particles. Since gas molecules are thermodynamically and kinetically unstable, these nucleation and growth processes occur rapidly in a relatively uncontrolled fashion compared to colloidal methods.

In order to produce vapor supersaturation for NP fabrication, various approaches have been employed using either solid, liquid or vapor precursors. For solid precursors, targets are vaporized into gas molecules by inert gas condensation,[39] pulsed laser ablation,[40] spark discharge[41] or ion sputtering.[42] In case of liquid or vapor precursors, various methods including chemical vapor condensation, thermal plasma, photothermal or laser pyrolysis. Although these syntheses take advantage of a wide range chemical precursor that are allowed to form multi-component NPs in the gas phase without template, they are still subject to a high degree of NP agglomeration and polydispersity, which can be overcome by capping ligands in the liquid phase.[38,43]

1.4.2.2. Liquid-phase

In contrast with harsh reaction conditions used in the vapor phase, wet chemical/colloidal methods have been proven to be the most favorable route for semiconductor NP fabrication due to better control of reaction parameters to produce phase pure and monodispersed particles. Besides, different ligands are utilized as a means of surface passivation to provide better control of the nucleation and growth processes. In general, classical La Mer model is used to explain the production process of monodispersed NPs in solution,[44] as described in Figure 1.5. In a typical colloidal synthesis, chemical reactants are quickly injected in a coordinating solvent solution at relatively high temperature (150-350°C)[45], creating unstable supersaturation in a confined space, resulting in formation of small intermediate nuclei. As high temperature is maintained, further consumption of precursors continually facilitates the growth of the particles. Due to the rapid addition of precursors, the nucleation process usually happen instantaneously, and is taken over by the precipitation of reactants on pre-established nuclei for further growth, thus no additionally new nuclei are produced. When the growth of all nuclei happens in the same way, uniform size distribution is observed over time. In other cases, a second growth phase called Ostwald ripening can occur, resulting in polydispersity in resulting nanoparticles. This particular process happens when the high-surface energy small nuclei dissolve back into solution and redeposit on the larger ones. Depending of the anisotropy of the crystal lattice, the growth dynamics along different directions are not similar.[46] Thus different reaction conditions such as temperature, time and the use of capping ligands can adjust the surface energy of the nanoparticles and provide better controllability of their growth kinetics.
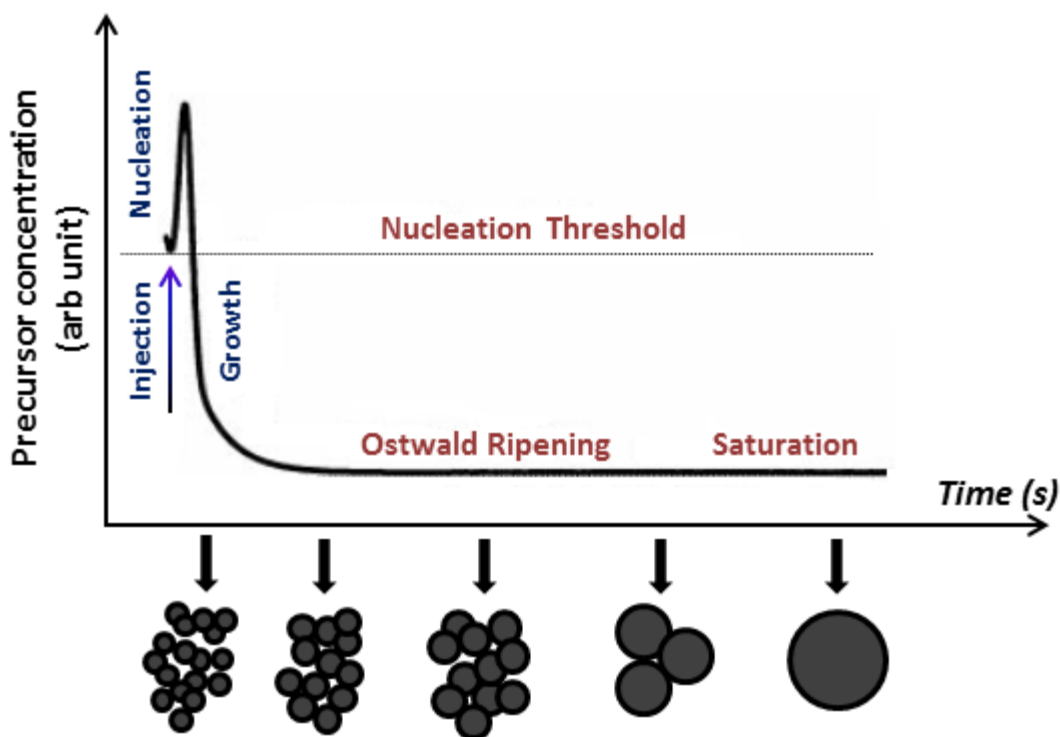
Figure 1.5. Scheme depicting the nucleation and growth stages in solution for the colloidal synthesis of monodispersed NCs in the framework of La Mer model.[45]

1.5.   Importance of Benign Semiconductor Nanomaterials

To date, many of the synthetic efforts are focused on II-VI (i.e. CdSe, CdTe, CdS),[47,48] IV-VI (PbSe, PbS, PbTe),[49,50] III-V (InAs, GaAs)[51,52] based semiconductors due to their relative ease of the synthesis and precise morphological control leading to basic understanding of photophysics. Accordingly, a number of potential applications have been suggested and successfully demonstrated.[53-55] However, one major problem with these materials is their inherent toxicity, which is detrimental to biological and environmental systems. In particular, studies have been demonstrated that the toxicity in cadmium-based quantum dots is due to the release or Cd^{2+} ions and/or formation of free radicals that can cause deadly effects on living cells.[56,57] Nevertheless, the

15

exceptional properties of semiconductor nanostructures and their promising application in a number of new technologies suggest the necessity to develop more environmentally benign materials that can potentially replace the existing highly toxic compounds.

1.6.   Group II-V Semiconductors

In contrast to the extensive studies on Group II–VI, IV–VI and III–V, the efforts on Group II–V NCs are rare although these materials exhibit much larger excitonic radii[58] that can potentially demonstrate pronounced size quantization[59,60] and molar absorptivities comparable to those of Group II–VI NCs.[61,62] Various fascinating magnetic,[63] structural[64] and electronic properties[65] were observed with these II-V narrow bandgap semiconductors, including Cd_3P_2, Zn_3P_2, Cd_3As_2 and Zn_3P_2. However investigations in their optical and optoelectronic properties have not been done systematically, with Cd_3P_2 nanostructures having been studied the most up to date. As a representative II-V semiconductor, Cd_3P_2 exhibits a small direct bandgap (0.55 eV)[66], with a large exciton Bohr radius (~36 nm),[59,67] high dielectric constant[68] and small electron effective mass.[69] Recently, Yu and coworkers prepared a series of Cd_3P_2 quantum dots, which have shown to be a promising class of light emitting material, with absorption tuned from 320 nm up to 1325 nm for NC sizes from 1 nm to 8 nm.[70] Along with Cd_3P_2, colloidal Cd_3As_2 quantum dots also showed exceptional luminescence from the visible to the IR region (530–2000 nm), which adds on to the availability applications for infrared emitters.[71]

Although possessing outstanding optical and electronic properties, most II–V semiconductor nanomaterials are composed of toxic elemental components (Cd, As), which limits their potential in commercial and biological uses. Among them, Zn_3P_2 is a more suitable option due to its environment-friendly nature and earth-abundance while retaining excellent properties of group II–V materials. In particular, bulk Zn_3P_2 exhibits an absorption coefficient on the order of 10^4 cm^{-1},[15,16] a carrier diffusion length of 5–10 μm,[72] and a direct bandgap of 1.4–1.5 eV[59,62] making it a promising candidate for solar cells,[73,74] light emitting diodes,[75] and lithium ion battery applications.[76] Accordingly, Catalano and co–workers demonstrated the use of polycrystalline Zn_3P_2 in Schottky–barriers[73] and Zn_3P_2/ZnO hetero–junction photovoltaic devices[74] with power conversion efficiencies up to ~6 %. Moreover, recent reports on Zn_3P_2 nanowire photoconductors[77] and solar cells[78] provide compelling evidence for the application of Zn_3P_2 in optical technologies. Despite its tremendous potential, the lack of well-developed chemical routes for crystalline and luminescent Zn_3P_2 nanostructures has led to inconsistent reports on size-dependent photophysical properties.

1.7. Group IV Semiconductors (Ge, Si)

In addition to Zn_3P_2, Group IV semiconductors (Si, Ge) have received less attention due to their inherent indirect bandgap structure.[79] However, there has been tremendous interest in the investigation of their optical properties due to their non- to less-toxic nature, high natural abundance and excellent compatibility with current Si–based electronic and photonic technologies.[36-41] To date, colloidal synthesis of high quality Si nanoparticles (NPs) with control over size and optical properties remains a challenging

task. Moreover, Si NCs are prone to oxidation by atmospheric oxygen, thus effective surface modification is required, making it a difficult material to work with. Top-down synthetic approaches produced Si NCs with control over size and emissivity that no other methods can do, but require relatively harsh conditions (HF etching) and high temperatures (>1200°C).[58,59] Bottom-up approaches have been shown to produce phase pure Si NCs with control over size but they exhibit much lower quantum yields and the full spectrum of colors were not attained.[60-65] Similarly, the synthesis of Ge NCs requires high crystallization temperatures (>250°C) and strong reducing reagents.[66-71] To date, the majority of the synthetic efforts for Ge NCs are bottom-up methods, in which functionalization of particle surface with organic ligands is required to prevent oxidation and aggregation. Reduction of Ge salts by sodium metals,[66-69] n-butyllithium (BuLi),[70,71] sodium naphthalide,[72-75] metal hydrides,[76-80] thermal decomposition[81-83] and reduction of organogermane,[84-89] are common strategies to synthesize colloidal Ge NCs.

The interest in production of $Si_{1-x}Ge_x$ alloy NCs arises from their miscibility at all compositions in the bulk,[95] similarity of electronic valency and low lattice mismatch.[30] Bulk Ge exhibit a bandgap of 0.67 eV, smaller than that of Si, 1.12 eV.[96] Alloying of these two elements in different compositions can tune their band energy in the intermediate range, potentially resulting in tunable absorption and emission.[97,98] Additionally, quantum confinement effect can blue shift the bandgaps of the $Si_{1-x}Ge_x$ nanoalloys, thus optical tunability spanning throughout the UV-visible to the near IR region can be obtained for the alloy NCs by adjusting size and composition. In addition, quantum confinement effect can possibly induce a quasi-direct gap behavior for

nanocrystalline $Si_{1-x}Ge_x$ alloys,[31] which will highly increase the molar absorptivity and emissivity of the NC product, making it a promising candidate for optoelectronic applications. However, $Ge_{1-x}Si_x$ alloy NCs so far have only been produced by high-energy synthetic routes such as thermal evaporation,[90] laser-induced[91] or non-thermal plasmas[92], using highly reactive and hazardous Si and Ge precursors (SiH_4, GeH_4, $GeCl_4$). Hence we propose to develop robust colloidal synthetic strategies for $Ge_{1-x}Si_x$ NCs with size and composition tunable bandgaps with promising absorption/emission properties, offering new perspectives for future optoelectronic applications.

1.8.   Thesis Statement

The two main goals that will be explored in this thesis are (1) to develop a moderately high temperature colloidal synthetic route for Zn_3P_2 and $Si_{1-x}Ge_x$ NCs with precise control over structure, morphology and composition (2) along with investigation of their size- and composition- optical properties as a function of synthetic parameters.

The initial motivation for a wet-chemical synthesis of Zn_3P_2 NCs is due to its cost-effective fabrication, and high control over size and dispersity by manipulation of nucleation and growth kinetics. In addition, the lesser number of literature reports in colloidal method, along with their varying structural and optical characterizations, add more interest in the investigation of their size tunable absorption and emission properties. Although earlier reports were able to probe the photoluminescence of Zn_3P_2 nanoparticles more than a decade ago, it was not until recently Luber and co-workers confirmed the tetragonal structure of non-luminescent Zn_3P_2 NCs. Therefore, this thesis fulfills the need of a robust colloidal synthesis of crystalline, luminescent Zn_3P_2 NCs and

optimization of their size-dependent optical properties controlled by fine tuning of reaction parameters.

Secondly, the interest to fabricate $Si_{1-x}Ge_x$ alloy NCs stems from high miscibility of Ge and Si, along with their capability to exhibit tunable absorption and emission throughout much of the visible to near-IR region via fine tuning of elemental compositions. Due to quantum confinement effect in the nano-regime, Ge and Si have shown some promising luminescent capacities, which are not normally observed in indirect gap materials. In the last decade, numerous reports have demonstrated the emission properties of Ge and Si nanoparticles prepared using different methods. However, Ge still exhibits limited size control and optical tunability, and the results obtained for Si remain inconclusive due to high influence of surface properties and its proneness to oxidation.[80,81] With bandgaps of 1.1[82] and 2.8 eV[83] experimentally achieved for ~5 nm Ge and Si nanoparticles, respectively, fabrication of nanocrystalline $Si_{1-x}Ge_x$ alloys can enable the compositional tunability of luminescence across the visible to the near-IR spectrum, offering them more promising future in optoelectronic applications. This thesis explores a wet-chemical route to make nanocrystalline $Si_{1-x}Ge_x$ alloys and examine the alloying and quantum confinement effects on their optical tunability and efficiency.

CHAPTER 2

CHARACTERIZATION TECHNIQUES

Different characterization techniques are specifically employed to gain better understanding about the properties (structural, chemical, optical, etc.) of NC products. In a wet-chemical synthesis, different reaction parameters (injection temperature, growth time, solvent use, etc.) can influence the complete reduction of chemical precursors into the desired compound, which can result in metal impurities as byproducts. In addition, the use of different surfactants and their amounts can affect the coating efficiency of prepared nanoparticles, which can influence the surface oxidation that leads to metal oxide impurities. In order to determine the phase purity of a material sample, powder X-ray diffraction (PXRD) analysis is employed to determine the crystal structure of as-prepared NCs. Utilizing Scherrer equation, Bragg reflections in the PXRD pattern can also be used to estimate the crystallite sizes of NC products. To confirm the chemical makeup of the material compound, compositional analysis utilizing scanning electron microscopy (SEM) coupled with an energy dispersive spectroscopy (EDS) is proven helpful for air-stable material. Further surface properties are explored by employing thermogravimetric analysis (TGA), Fourier transform infrared (FT-IR) and X-ray photoemission spectroscopy (XPS). These investigations are essential to gain better understanding of the surface chemistry of as-prepared products, which play an important role in many of their intrinsic properties. For microscopic studies of resulting NCs, transmission electron microscopy (TEM) is a most common technique used to

estimate the size, shape and their lattice fringes, which are important to confirm the identity of the material. Finally, solution absorption and photoluminescence spectroscopy are used to study the optical properties of the prepared NC products dispersed in a non-polar medium, and diffuse reflectance analysis is utilized for solid powder samples. These optical investigations can determine the effect of size confinement effect on the absorption and emission energy of the resulting NCs. In addition, PL quantum efficiency will also be estimated with regards to a standard organic dye and band-edge emissions can be confirmed by time-resolved PL studies.

2.1. Powder X-ray diffraction (XRD)

In order to gain a better understanding about the phases and crystal structures of prepared materials, PXRD is common choice among many analytical techniques. Each and every crystalline material possesses a diffraction pattern that is characteristic to its particular crystal phase, and it serves as a "fingerprint" structural feature for that material. Since X-ray radiation wavelengths are in the same order of the crystal inter-atomic distances, electrons in atoms create strong scattering effects with the oscillating electric field of the X-ray, resulting in diffractions. In the crystal form, several atoms assemble themselves into multiple periodic arrays, thus X-ray diffraction from different planes of atoms provide information of the atomic arrangement and crystal structure of the material.

In a typical PXRD instrument, an X-ray tube is used to generate the X-rays by applying an accelerating voltage and allowing the electron beam to interact with a metal target (e.g., Cu). A high voltage of 30,000 – 50,000 volts is used to heat a tungsten

filament, resulting in ejection of highly energetic electrons (Figure 2.1). When these incident electron beams interact with the Cu target, ionization happens by the removal an electron from the Cu 1s orbital (K shell). This vacant spot will be replace by electron either from the 2p or 3p outer shell, These electronic transitions release energies that are characteristic of the X-ray generated of Kα (2p – 1s transition) and Kβ (3p – 1s transition). Depending on which orbital the electrons come from, X-rays are categorized in two kinds of Kα (2p) or Kβ (3p).
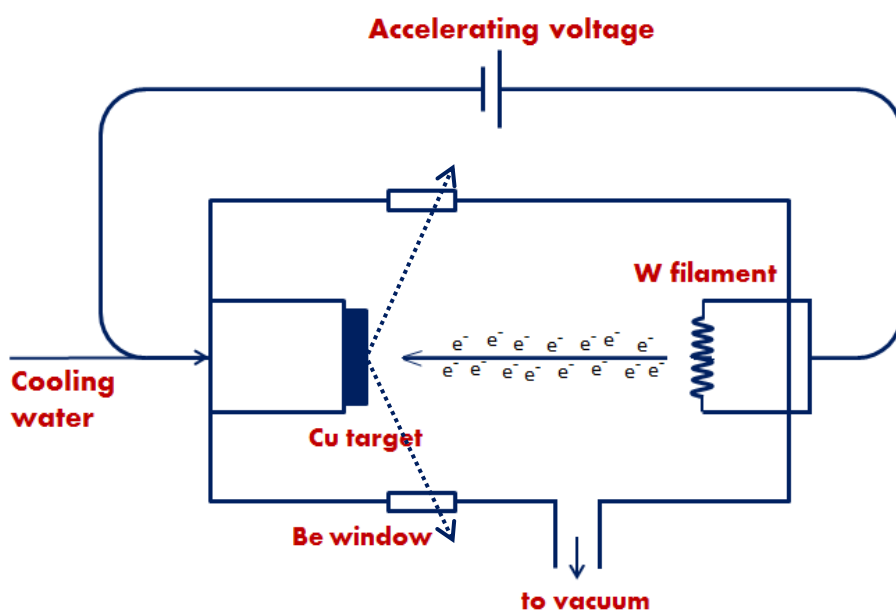
Figure 2.1. A typical X-ray tube in PXRD instrument using Cu Kα radiation (λ = 1.5418 Å) (adapted from Cullity).[84]
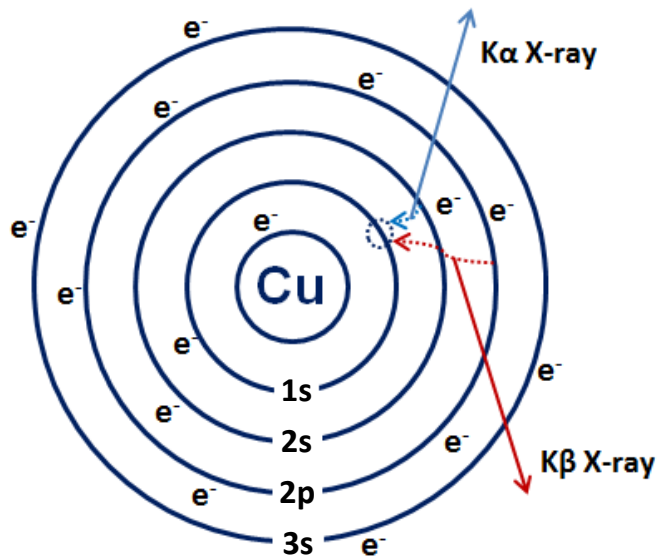
Figure 2.2. Diagram showing the formation X-ray radiation from Cu target, which occurs due to ionization of the 1s electron, followed by the replacement of an electron either from 2p or 3p orbitals resulting Kα or Kβ radiation, respectively (adapted from West).[85]

In general, the higher energy Kα radiation is used for all PXRD experiments, and the lower energy Kβ is filtered away by a monochromator. Upon hitting the sample of interest, part of the X-ray beam is reflected off the surface plane in a mirror-like manner at an angle equal to incident one, while other part is transmitted into the inner planes. The distance these beams travel deeper into the crystal are dependent on the lattice spacing d of two consecutive planes. Consider there are two beams A and B coming into contact with the sample. X-ray A gets diffracted off the surface plane as A', and beam B penetrates thought the 1ˢᵗ plane and is diffracted as B' (Figure 2.3). The two consecutive planes are separated by a distance of d-spacing. X, Y, Z are contact points generated by the 2 incident beams. In the case of constructive interference, the

additional distances XZ + YZ is an integral of the X-ray wavelength and the diffracted

angle is mathematically related to the d-spacing by Bragg's law (Eq. 2.1)

$$XY + YZ = n\lambda$$

$$\sin\theta = \frac{XY}{d} = \frac{YZ}{d}$$

$$2\sin\theta = \frac{XY+YZ}{d} = \frac{n\lambda}{d}$$

$$\Rightarrow \quad n\lambda = 2d\sin\theta \qquad\qquad (2.1)$$
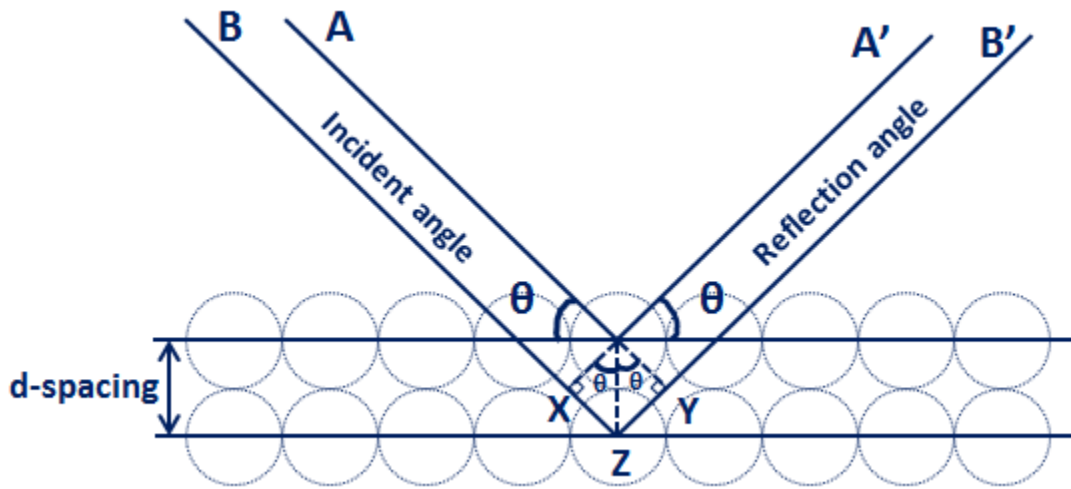
Figure 2.3. Schematic illustration of the diffractions of X-ray beams interacting with two

consecutive crystal planes in a solid sample.

In order to satisfy Bragg's law, crystallinity of the powder sample is necessary, so

that diffracted waves can give rise to peak intensity and pattern information regarding

structure of the crystal. The constructive interference result in diffraction peak intensity

which is plotted against 2θ. The diffraction peak positions represent a particular pattern

that is specific to the size and shape of the crystal unit cell. The compositions and how

every atom is positioned in the unit cell result in different peak intensities. When it

comes to materials, PXRD patterns in bulk and nanoscale differ from each other in the peak broadness. Nanocrystallites compose of much smaller number of lattice planes than the bulk, thus partially interfering waves are not completely cancelled, resulting in broader diffraction peaks. The broadness of the peaks are inversely proportional to the crystallite size and determined by Scherrer equation 2.2

$$t = \frac{0.9\,\lambda}{B\cos\theta} \tag{2.2}$$

where t is the size of crystal, λ is the X-ray wavelength used, B is the full width at half maxima of the peak, and θ is the diffraction angle. This calculation only allows for determination of the average crystal size, and might be different from size calculated from other spectroscopic or microscopic techniques, mainly due to the present of surfactants or materials coating the crystal surfaces.

In this study, A Philips X'Pert system equipped with a Cu Kα radiation (λ = 1.5418 Å) was used to record powder X–ray diffraction (PXRD) patterns of all samples. The crystallite sizes were estimated by employing Scherrer equation,[86] after making appropriate corrections for instrumental broadening using a Si standard. The powder sample is prepared by depositing on a low background Si holder. Analyzed X-ray diffraction patterns are compared against the International Centre for Diffraction Data (ICDD) powder diffraction file (PDF) database for identification of crystal phases.

2.2.   UV-Visible Absorption Spectroscopy

Among analytical techniques, this is one of the oldest and most popular techniques used to investigate the optical properties of compounds under the influence of photon

energy. For solution absorption spectroscopy, compound molecules are dissolved in an optically transparent solution. When ultraviolet or visible light pass through these molecules, part of this energy is absorbed and part is transmitted through solution. The transmitted part gets detected and is mathematically transformed to determine the absorbance value of the solution. The intensity of the absorption is directly proportional to the concentration of the analyte (c), the molar absorptivity (ε) and path length (l) of the sample holder by the Beer-Lambert law

$$A = \varepsilon \, l \, c \tag{2.3}$$

In this equation, the absorptivity is highly related to the structure of the analyzed molecule. In semiconductor materials, absorption of light results in the transition of electrons from the VB to the CB, and the wavelength maxima of the absorption peak can be correlated to the bandgap energy of the material. Since the bandgap energy increases with smaller crystal size due to the quantum confinement effect, absorption maxima are blue shifted relative to the bulk and with respect to decreasing crystal size. Absorption spectra are generally broad owing to the presence of several vibrational and rotational levels within the electronic levels. In this thesis study, this technique was utilized to examine the size-dependent optical bandgaps of the resulting semiconducting NCs. Typically, purified samples were dispersed in non-polar medium (chloroform, CCl_4) and contained in quartz cuvette prior to being analyzed. All solution absorption spectra were collected by a Cary 6000i UV–vis–NIR spectrophotometer (Agilent Technologies) equipped with tungsten and deuterium sources. Instrumental parameters such as slit width and cell path length were kept constant through all experiments. Figure 2.4

illustrates a typical set up of an absorption spectrophotometer equipped with a photodiode array detector.
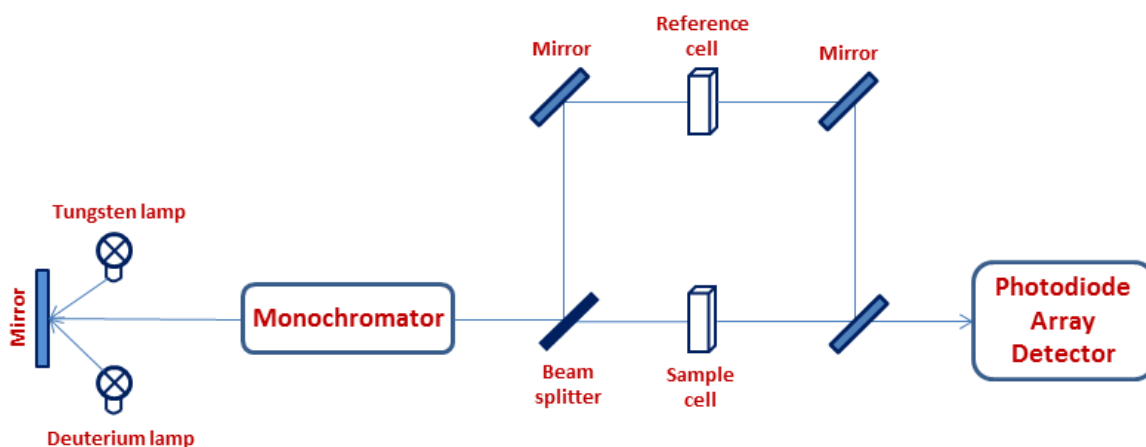
Figure 2.4. A simple schematic diagram of a typical double beam UV-Vis Spectrophotometer utilizing Tungsten and Deuterium sources and a PDA detector.

2.3. Solid State Diffuse Reflectance UV-Visible Spectroscopy

For powder samples that are insoluble in either organic or aqueous media, diffuse reflectance technique is used for analysis instead of the more common solution absorption method. When ultraviolet or visible light interacts with a solid sample, there are two types of reflections, specular and diffuse, that can occur besides transmission and absorption. When incident beam reflects directly off a smooth sample surface in a mirror-like manner, it gives rise to specular reflection. More often, radiation will interact with a rough solid surface and partially penetrate into the sample, leading to subsequent absorption, reflection and diffraction of light in all directions. These diffusively scattered

beams are collected for analysis since they retain the optical information of the analyte of interest, and this is the principle of the diffuse reflectance technique.

To quantitatively evaluate the reflectance data, the Kubelka-Munk remission function is a widely applied method to obtain pseudo-absorption information of the material (eq. 2.4)

$$f_{KM}(R) = \frac{(1-R)^2}{2R} = \frac{K}{S} \tag{2.4}$$

where R is the percentage diffuse reflectance of the analyte to that of the non-absorbing reference, K is the molar absorption coefficient and s is the scattering coefficient.[87,88] The optical energy gap information of the material is obtained from the linear extrapolation of the absorption onsets to the baseline intersection point. In addition to Kubelka-Munk, there are other methods used for acquiring the optical absorption of nanomaterial from diffuse reflectance spectroscopy. Among those, Tauc analysis is the one that accounts for the difference in electronic transitions for both direct and indirect gap semiconductor materials. In semiconductors, electronic transitions are subject to specific selection rules depending on the crystal momentum of the band structure. As mentioned in Chap 1, whether the band structure is considered to be direct or indirect essentially depends on whether the photon-assisted transition is conserving its momentum. Thus the Tauc analysis demonstrates the proportionality between the absorption coefficient (α) and the available density of states ($h\nu - E_g$) for a particular transition by eq. 2.5

$$(\alpha h\nu)^n = A(h\nu - E_g) \tag{2.5}$$

where A is the proportionality coefficient, hv is the photon energy and E_g is the bandgap. The value of n (1/3, 1/2, 2 or 2/3) is determined by the interband transitions of indirect forbidden, indirect allowed, direct allowed or direct forbidden, respectively. Similar to Kubelka-Munk method, the bandgap energy values can be also obtained from Tauc analysis by the baseline intersection with the linear regression of the absorption onsets acquired from $(\alpha h v)^n$ vs hv plot.

For this method to work efficiently, excessive amounts of a non-absorbing matrix (e.g. $BaSO_4$) are used for sample dilution in order to allow higher penetration of the incident beam into the sample matrix and eliminate the interferences coming from the specular reflection phenomenon. Typically, a dried powder sample is homogeneously mixed with $BaSO_4$ powder to form a pellet prior illuminating it with UV-Vis beam. For this thesis experiments, a Cary 6000i UV–vis–NIR spectrophotometer (Agilent Technologies) equipped with an internal DRA 2500 attachment was used to perform the reflectance measurements. This technique serves as a complimentary one to the solution UV-Vis absorption technique in order to explore the optical bandgaps and particle size relationship under quantum confinement effects.

2.4. Photoluminescence Spectroscopy

Photoluminescence (PL) is generally referred to as an emission of light by excited molecules that absorb energy from an excitation source. This process is depicted in Figure 2.5, and it can also be considered as the result of radiative recombination of electron-hole pairs in a semiconductor material. In general, the ground state and excited state consist of many vibrational and rotational energy levels. Absorption of photon

energy excites molecules from singlet ground state (S_0) into the 1st singlet excited state (S_1), followed by the relaxation of electrons from S_1 to S_0, accompanied by the release of photons (Figure 2.5) This radiative process results in fluorescence energy that is characteristic of the material. In case absorption energy exceed that of difference between S_1 to S_0, this excess energy promotes molecules to higher vibrational levels, followed by their relaxation via non-radiative processes (heat) before reaching the ground state. When pholoholuminescence happens, there is an intersystem crossing of molecules from excited singlet to triplet excited states, followed by relaxation to ground state at a much longer wavelength. This process happens when there is a presence of impurity, defect or a foreign species, whose energy levels are in similar order of S_1. Excited molecules from S_1 cross over into these excited T_1 states before decaying into S_0, resulting in a red shift in energy compared to fluorescence. In general, emission wavelengths are red shifted relative to absorption ones, owing mostly to non-radiative vibrational relaxation of excited electrons known as Stokes shifts.
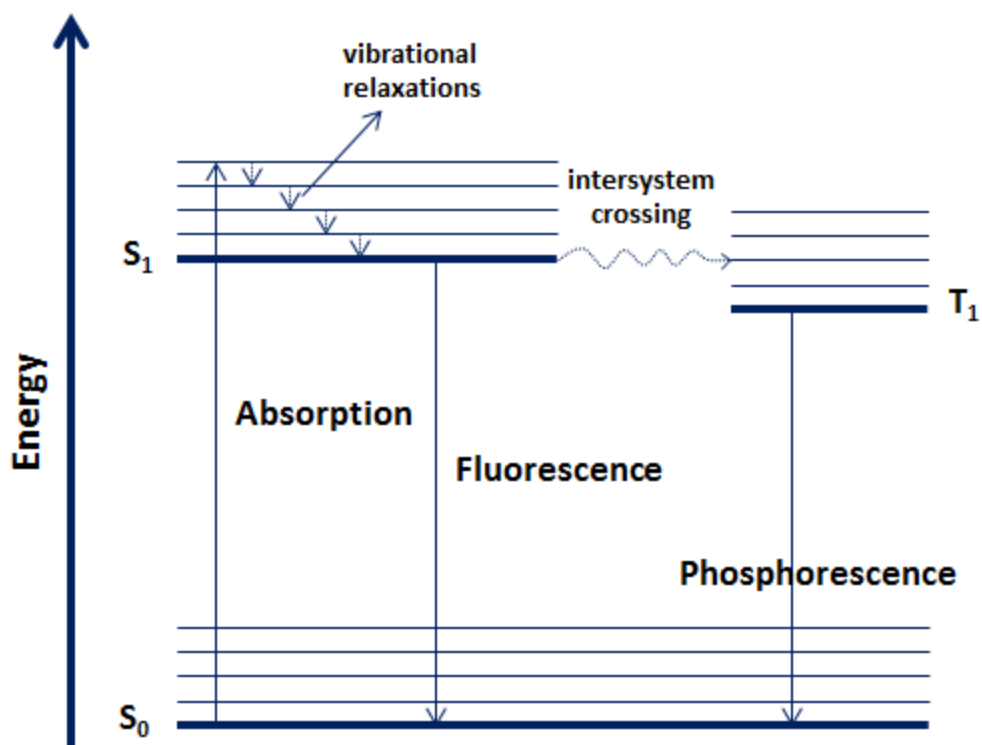
Figure 2.5. A schematic illustration of absorption followed by fluorescence and phospholuminescence processes under the effect of light energy.

Along with absorption spectroscopy, PL spectra are used to investigate the size-dependent optical properties of semiconductor NCs. All emission spectra were excited at the photoluminescent excitation (PLE) maximum. In addition, relative emission quantum efficiency can also be deduced from this technique. In this thesis study, The PL QYs were measured relative to a standard dye, Rhodamine 6G. The optical densities of NC samples and Rhodamine 6G in $CHCl_3$ were adjusted to 0.08 and the emission spectra were recorded with the same excitation wavelengths. The quantum yields were calculated based on the comparison between integrated emission spectra of NC samples and Rhodamine 6G under identical experimental conditions. All PL measurements in this thesis are performed using Cary Eclipse fluorescence

spectrophotometer (Agilent Technologies) equipped with a xenon arc lamp that produces continuous wavelengths from 200 to 800 nm.

2.5. Time-Resolved Photoluminescence (TR-PL)

This technique has been of rising demand recently owing to the development of various laser sources covering a wide range of energy and wavelength tunability.[89] As mentioned above, semiconductor photoexcited excitons may undergo different modes of recombination, resulting in either radiative or non-radiative relaxation. When it comes to NCs, surface moieties or defects give rise to mid-gap states which are able to trap the photoexcited excitons, thus inhibiting band-edge recombination. Utilizing ultrashort pulse laser, TR-PL spectroscopy allows probing more information about the relaxation pathways of charge carries in nanomaterials. For all luminescent sample prepared in this study, TR-PL measurements were performed using a frequency tripled Ti:sapphire laser (267 nm wavelength, 150 fs pulse width, 80 MHz repetition rate) and a Hamamatsu streak camera with 25 ps temporal resolution. The samples drop-casted on silicon substrates were mounted on a closed-cycle He cryostat for measurements at 10 K.

2.6. Transmission Electron Microscopy (TEM)

This is the most widely used microscopic technique for determination of the general morphology and structure of nanomaterials. For this technique, electrons are used instead of light for imaging purpose due to their fine tunability of wavelengths that can be controlled by an applied electric field. When an electron beam is allowed to hit a

substrate, multiple events can occur and each of them carries different information regarding the analyzed species (Figure 2.6). Among them, TEM utilizes the transmitted beam to gain more information regarding the nanomaterial size, shape and morphology. High resolution TEM can further determine the lattice fringes, which are specific fingerprints of a specific material. This information plays an important role in helping with the identification of the material crystal structure.

In a typical TEM instrument, a tungsten filament crystal is often used as the source, which can be thermally or electrically excited to emit electrons with applied electric field. During an analysis, high voltages of 100–400 kV are applied and can be adjusted to control the wavelength of generated electrons. For a typical imaging operation, the sample is deposited on a copper grid coated with a thin layer of carbon, and residual solvent is allowed to evaporate prior to being analyzed. One of the most important things that need to be considered before using this technique is confirming the sample transparency and stability under the electron beam. For a simple mode TEM analysis, both transmitted and diffracted electron beams are utilized, and the imaging process is aided by the use of different optical lenses which help constructing the image and diffraction patterns. During an experiment, imaging and diffraction modes can be switched between each other in order to either obtain the general morphology of the particles or the lattice information about the crystals.
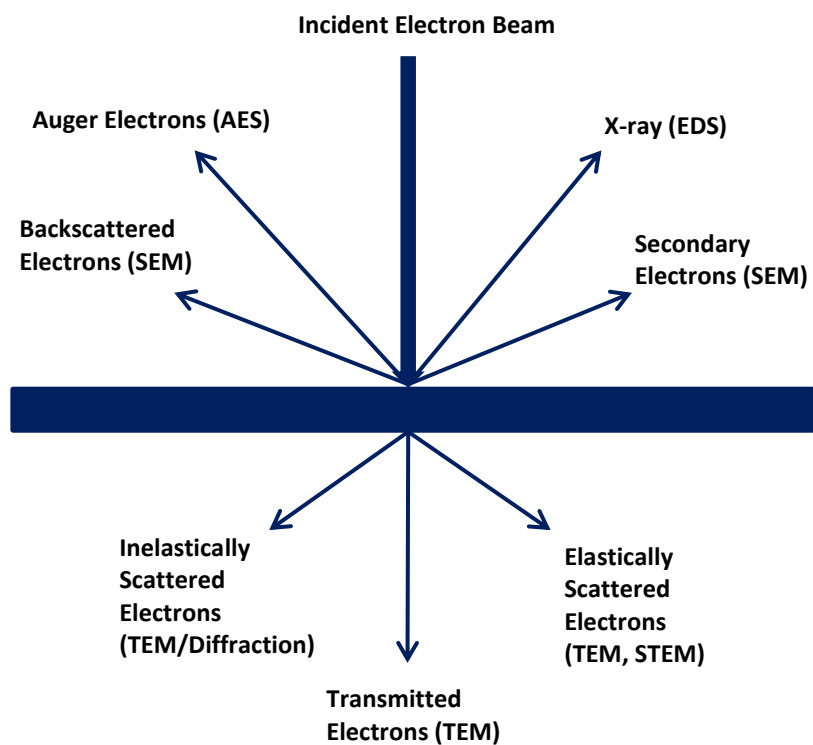
Figure 2.6. Different interactive phenomena of an electron beam with a solid material substrate.

For experiments performed in this thesis study, a Zeiss Libra 120 with a Gatan ultrascan 4000 camera operating at 120 kV is utilized for low-resolution imaging, and high–resolution TEM images were recorded on a FEI Titan 8300 electron microscope equipped with a Gatan 794 multiscan camera operating at 300 kV.

2.7. Scanning Electron Microscope – Energy Dispersive spectroscopy (SEM-EDS)

As shown in Figure 2.6 above, a high energy electron beam can have several interactions with the sample, and the reflected or transmitted beams can provide

different information regarding chemical or physical properties of the analyte. When a scanning electron microscope is coupled with an energy dispersive spectroscopy, an electron beam is scanned across the analyte surface, and a variety of signals are generated from the sample. When the beam creates a vacancy in the material molecule orbital, an electron is transferred from outer orbital to fulfill that spot, resulting in an emission of an X-ray beam characteristic of that element. Elements possess different characteristic atomic structures, which cause their emitting X-ray wavelengths to be different. This technique is can quantitatively and qualitatively help in identification of the elements present on the surface of the sample of interest. A Hitachi SU–70 SEM-EDS instrument is utilized for these characterizations. Sample preparation involves deposition of sample onto conducting carbon tape before putting under vacuum for analysis.

2.8. X-ray Photoemission Spectroscopy (XPS)

This is another powerful analytical technique to determine the surface elemental compositions of materials, and it is often called Electron Spectroscopy for Chemical Analysis (ESCA). It works by the bombardment of the sample with a monoenergetic X-ray beam causing the ejection of electrons of from the surface atoms with discrete energy levels. The conservation of energy in photoemission is

$$E_{hv} = E_k + E_\Phi + E_B(i) \tag{2.5}$$

where E_{hv} is the X-ray energy, E_k is the photoelectron kinetic energy, E_Φ is the work function and $E_B(i)$ is the electron binding energy in the (i^{th}) level. When E_Φ is constant for particle analyzer, and E_k is determined by electron analyzer, then $E_B(i)$ can be

calculated based on the above relationship. Elements possess different atomic structures, and electrons in the core orbitals experience different nuclear forces (binding energy). In addition, atom of the same element does not necessarily have the same binding energies because it can be altered by the surrounding chemical environment. For example, when valence shell electrons are removed, oxidation state of the atom becomes more positive, there is less shielding effect imposed on the core electrons, thus increasing the binding energy. Besides oxidation states, ligand electronegativity, coordination effects are also parameters that can influence chemical shifts in binding energies. With this capability, XPS is an essential technique to investigate many surface-related properties. Since surface atoms play much more important roles in nanomaterials, XPS has become one of the most important characterization techniques to investigate size-dependent photophysical properties of semiconductor NCs. For experiments involved in this study, a Thermofisher ESCALAB 250 instrument equipped with an Al Kα source was used for all the XPS measurements. As-prepared samples are spread on a piece indium foil deposited on conducting carbon tape in order to account for the surface charging effect of the instrument, which can create a shift in the binding energy. XPS spectra are collected with peaks representing different binding energies of surface compounds. Due to the overlapping in binding energies of different compound oxidation states, deconvolution analysis was performed to precisely determine assign the appropriate peaks for different species.

2.9. Thermogravimetric Analysis (TGA)

This technique is commonly used to monitor the change in mass of material as a function of temperature under an inert atmosphere (He, N_2 or Ar). Typically, thermal decomposition of the solid sample is a complex process, which involves several physical and chemical changes of the material, as it reaches high temperature (600–700°C), such as sublimation, vaporization, liquidation, crystal phase change, desorption, etc. For example, desorption of surface solvents or surfactants from as-prepared sample can happen differently and proceed in stage-like processes. Depending on the boiling point and binding affinity of those molecules on the materials, their desorption temperatures can vary significantly, and this evidence can reveal partial information about the effectiveness of the capping molecules. Besides that, TGA has often used to monitor the thermal and oxidative stability along with relative composition of multi-component systems. For these studies, samples were deposited on a platinum pan and loaded in into a furnace under N_2 flow. Typical TGA curves were recorded at heating rate of 10°C / min and terminated at 600°C.

2.10. Fourier Transform Infrared (FT-IR) Absorption Spectroscopy

Infrared (IR) spectroscopy generally involves low-energy transitions between vibrational or rotational energy levels. In order to absorb IR radiation, the compound must undergo a net change in dipole moment under induced vibrations. With the use of the interferometer and Fourier transform data processing, FT-IR has been proven a convenient, fast and non-destructive technique for material characterization. Figure 2.7 represents a simple illustration of a typical FT-IR set-up, which includes a) the Nernst

glower source, b) the Michelson interferometer, and c) the triglycine sulfate pyroelectric detector. The interferometer contains a KBr beam splitter, a fixed and a moving mirror, which is essential for the generation of an interferogram. Due to the high surface-to-volume ratio of nanomaterials, FT-IR is one of earliest and most popular techniques used for monitoring the surface chemical activities. Since most molecular vibrations are dependent on the surrounding chemical bonds involved, each molecule exhibits a specifically unique vibrational absorption frequency that serves as a '"fingerprint" spectral feature associated with it.[90] Nowadays, a common use of FT-IR in nanoparticle characterization is the identification of specific functional groups associated with the surface-bound solvents or surfactants. This investigation leads to better understanding about the effect of passivating ligands on the resulting nanoparticles. All IR spectra are collected using a Nicolet 670 FT–IR instrument equipped with a single-reflection diamond ATR attachment. For this set-up, IR radiation undergoes total internal reflection as it passes through an internal reflection element (diamond). The reflected beam interacts with the sample/diamond interface and is capable of penetrating a short distance into the sample surface, resulting in absorption.
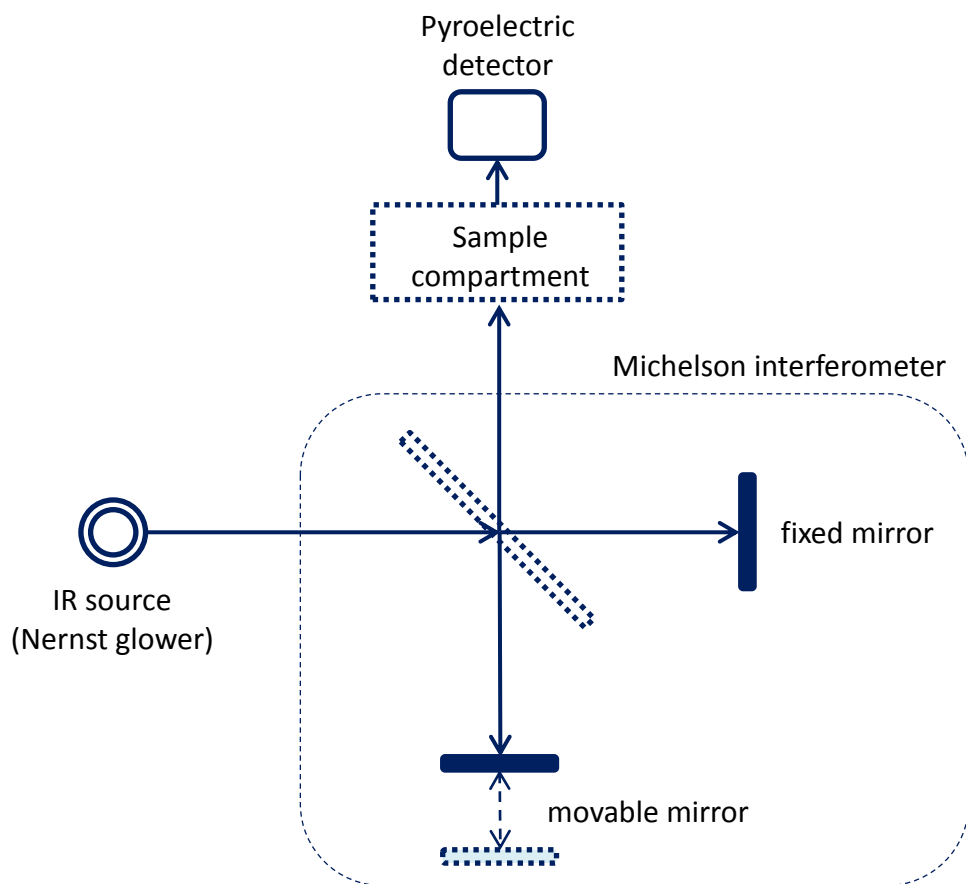
Figure 2.7. A typical FT-IR set-up utilizing a Nernst Glower source, a Michelson interferometer and a pyroelectric detector.

CHAPTER 3

Size–Dependent Optical Properties of Luminescent Zn_3P_2 Quantum Dots

3.1. Introduction

To date, a number of synthetic methods for the production of Zn_3P_2 nanostructures have been reported, of which the majority rely on chemical vapor deposition or electrodeposition methods[91-99] but fewer are based on wet chemistry[59,60,78,100-102] The initial dominance of deposition methods can be attributed to applicability of Zn_3P_2 as a promising material in solar cells, which require fabrication of thin films. Nonetheless, wet chemical syntheses have an edge over other synthetic routes owing to low production and post–synthetic processing costs, greater size and size dispersity control, and potential control over crystal structure and composition. However, numerous efforts on the wet chemical synthesis of Zn_3P_2 resulted in conflicting reports on the structure and optical properties.[59,60,100,101] For instance, Weller and coworkers claimed the synthesis of luminescent Zn_3P_2 nanoparticles (NPs) with quantum yields (QYs) up to 15%.[100] However, the structural characterization of the product was not supported by powder X–ray diffraction or electron microscopic studies.[100] Later, Green and O'Brien described the synthesis of luminescent Zn_3P_2 with no proof of crystal structure.[59] Recently, Miao et al. reported the synthesis of nonluminescent Zn_3P_2 NPs using zinc stearate and $P[Si(CH_3)_3]_3$.[60] Although emission was observed for nanostructures prepared with other

precursors (diethyl zinc and PH_3), the authors attributed it to Zn_3P_2/ZnO core/shell NPs.[60] More recently, Glassy et al. described the synthesis of Zn_3P_2 using multiple precursors with insight on the growth mechanism supported by NMR spectroscopy.[101] While the NPs are reported to exhibit distinct excitonic transitions, the emission properties were not thoroughly examined.[101] In contrast, recent wet-colloidal syntheses have resulted in high quality tetragonal Zn_3P_2 crystallites with no indication of the size-dependent optical properties.[78,102] These varying reports on nonluminescent crystalline and structurally uncertain luminescent Zn_3P_2 emphasize the need to develop robust and reproducible syntheses for phase-pure crystalline and luminescent Zn_3P_2 NPs.

3.2. Experimental

3.2.1. Synthesis of Zn_3P_2 NCs in HDA/ODE

In a typical experiment, 1-hexadecylamine (HDA) was placed in a three–neck flask with a condenser, septum, and thermocouple attached and dried under vacuum at 110 °C for 1 h. Then, the flask was flushed with argon, and the temperature was raised to 300 °C. In a nitrogen-filled glovebox, two mixtures of 0.05 mmol tris-(trimethylsilyl)phosphine (($TMSi)_3P$) in 1.00 mL of 1-octadecene (ODE) and 0.105 mmol of Et_2Zn in 1.00 mL of ODE were prepared separately prior to the synthesis. When the temperature of HDA reached 300 °C, colorless solutions of $(TMSi)_3P$/ODE and Et_2Zn/ODE were quickly and simultaneously injected under vigorous stirring and continuous argon flow. Upon injection, the temperature of the reaction mixture dropped to 265–272 °C and was allowed to ramp up to 300 °C within 3–4 min. To prevent the loss of phosphorus due to evaporation of $(TMSi)_3P$, the argon flow was stopped right

after the injection, and the reaction flask was kept under reflux at 300 °C. Zn_3P_2 NCs with sizes in the range of 4.8 ± 0.7 – 8.8 ± 1.3 nm were grown at 300 ºC for 15–90 min. After the desired growth time, the reaction was quenched by blowing compressed air until the temperature reaches below 100 °C and 5 mL of toluene was added. As–prepared NCs were isolated by solvent precipitation with methanol followed by centrifugation to achieve a yellow–orange to reddish–brown precipitate and purified by multi–step redispersion and reprecipitation in chloroform and methanol, respectively. Finally, the purified Zn_3P_2 NCs were dispersed in anhydrous chloroform to produce stable colloidal solutions.

In addition to the synthesis of Zn_3P_2 at different time intervals (15–90 min.) at 300 °C, NCs were also grown at different reaction temperatures (230–300 °C) for a fixed growth time (60 min.) to systematically investigate the evolution of optical properties. In this study, $(TMSi)_3P/ODE$ and Et_2Zn/ODE precursor solutions were quickly injected to dried HDA at the desired nucleation temperature and the resultant nuclei were grown for 1 h at the same temperature. The isolation and purification of NCs were performed as described above.

3.2.2. Synthesis of Larger Zn_3P_2 Crystallites

The synthesis of larger Zn_3P_2 crystallites was carried out in 100% ODE without the use of HDA surfactant. In a typical synthesis, 5 mL of ODE was dried under vacuum at 110 °C for 1 h, and the temperature was raised to 300 °C. At 300 °C, two mixtures of Et_2Zn/ODE and $(TMSi)_3P/ODE$ were rapidly and simultaneously injected under continuous argon flow. The reaction mixture was maintained at 300 °C for 30 min before cooling down with compressed air, and the resulting dark brown precipitate was washed

with toluene and methanol, followed by drying under vacuum prior to further characterization studies.

3.3.   Results and Discussion

The synthesis of Zn_3P_2 NCs was carried out by employing the hot injection method using Et_2Zn and $(TMSi)_3P$ as zinc and phosphorus sources, respectively. The larger Zn_3P_2 crystallites were prepared in high boiling, non-coordinating alkene solvent (i.e. ODE) whereas the smaller NCs were produced in HDA/ODE surfactant/solvent mixtures. Initially, the larger particles were synthesized to prove that the material, which is being produced by the reported method, is phase-pure tetragonal Zn_3P_2. The second motive is due to controversial results reported from recent studies on luminescent Zn_3P_2 NCs,[60,101] which exhibit conflicting powder diffraction patterns. Accordingly, larger Zn_3P_2 particles were produced in ODE via hot injection of $(TMSi)_3P$/ODE and Et_2Zn/ODE at 300 °C, followed by the growth of the resultant nuclei for 30 min. Since the precipitation of particles has already occurred, the reaction product was colloidally unstable and no further solution-based characterizations could be employed. However, the powder diffraction patterns of the precipitate indicate the formation of phase–pure tetragonal Zn_3P_2 (JCPDS 01–073–4212) whereas the narrow and intense Bragg reflections suggest the growth of larger particles (crystallite size = 50–60 nm, Figure 3.1). Consistent with the diffraction data, the elemental analysis of the reaction product using SEM/EDS confirmed the presence of Zn and P with atomic ratios of 55.3:44.7. The bandgap onsets determined by solid-state absorption spectra (Figure 3.2) are in the

range of 1.45–1.53 eV, which are consistent with the literature reports on bulk

tetragonal Zn_3P_2 (1.4–1.5).[59,62]
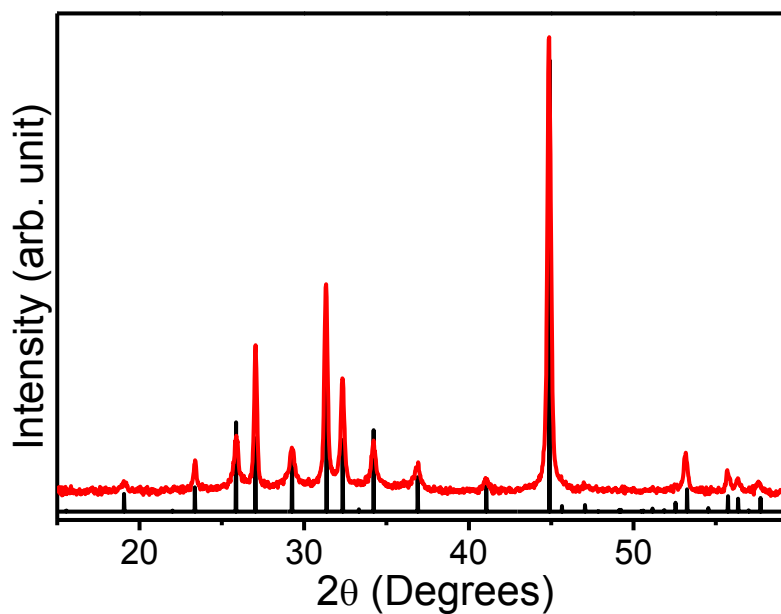
Figure 3.1. Powder X-ray diffraction pattern of the larger (~50–60 nm) Zn_3P_2 crystallites

produce in ODE at 300 °C for 30 min. ICCD–PDF overlay of tetragonal Zn_3P_2 (JCPDS

01–073–4212) is shown as vertical black lines.
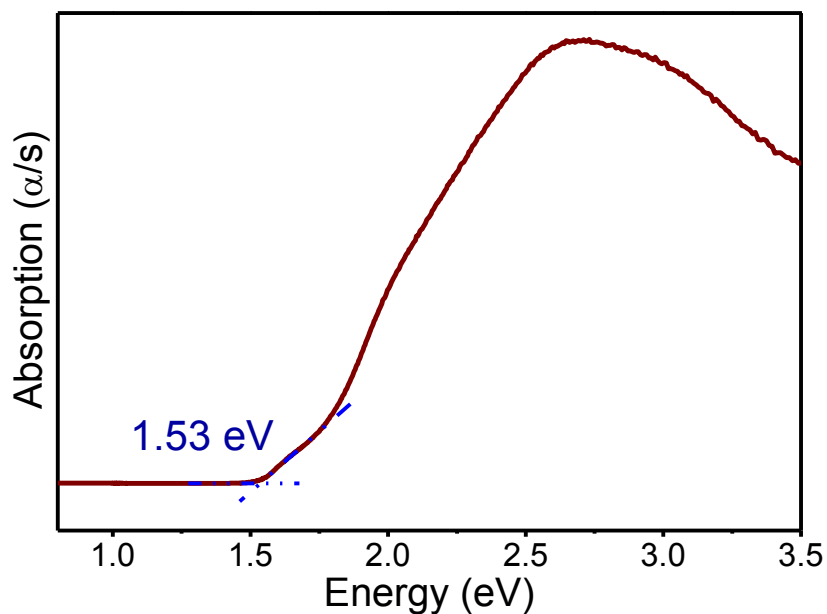
Figure 3.2. A representative solid state absorption spectrum of the larger (~50–60 nm) Zn_3P_2 crystallites produced in ODE at 300 °C for 30 min. Data acquired in the reflectance mode were converted to absorption using the Kubelka-Munk remission function.

Following the synthesis of the larger particles, the efforts were focused on achieving the size and size dispersity control by employing a high boiling amine surfactant (HDA) in combination with a noncoordinating alkene solvent (ODE). The use of HDA as the surface passivating agent was motivated by the high affinity of alkyl–amines for zinc chalcogenides.[103,104] Accordingly, ODE was used as the solvent of Zn and P injection mixtures, while HDA was used as the reaction medium. Upon simultaneous injection of two individually prepared $(TMSi)_3P$/ODE and Et_2Zn/ODE precursors to HDA/ODE at 300 °C, the reaction color changed from colorless to yellow, which gradually turned into orange and orange–red. The injection of individually prepared $(TMSi)_3P$/ODE and Et_2Zn/ODE mixtures was found to be critical for the formation of phase-pure tetragonal

Zn$_3$P$_2$. When a pre–mixed solution of (TMSi)$_3$P/Et$_2$Zn/ODE was employed in the synthesis, conflicting powder diffraction data were obtained, similar to recent reports on structurally uncertain, luminescent Zn$_3$P$_2$ NCs (Figure 3.3).[101] After the desired growth time at 300 °C, the reaction was quenched using compressed air, followed by the addition of toluene and isolation of NCs using methanol. The NCs synthesized in HDA/ODE were highly crystalline and exhibit excellent colloidal stability in nonpolar organic solvents due to the strong coordination of HDA to the NC surface. Accordingly, Zn$_3$P$_2$ NCs with average sizes in the range of 3.2 ± 0.6 – 8.8 ± 1.3 nm were produced by altering the injection/growth temperatures (230–300 °C) with a constant growth time (1 h) and also by varying the growth time between 15 and 90 min at 300 °C.
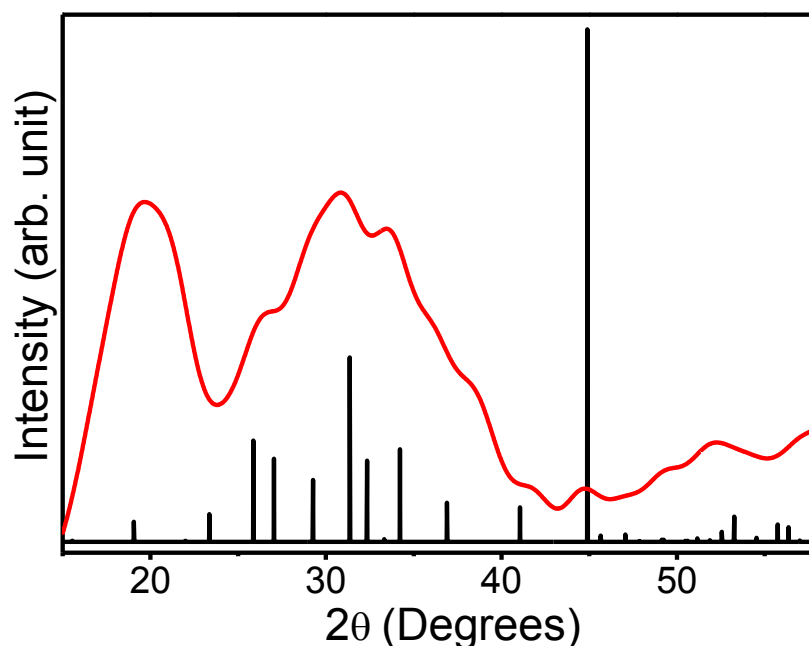
Figure 3.3. PXRD pattern of the product when a pre-mixed solution of (TMSi)$_3$P/Et$_2$Zn/ODE was injected in HDA at 300 °C and grown for 60 min. ICCD–PDF overlay of tetragonal Zn$_3$P$_2$ (JCPDS 01–073–4212) is shown as vertical black lines.

The phase purity of larger Zn_3P_2 crystallites and smaller NCs were investigated by employing the PXRD technique. As mentioned earlier, the dark brown precipitate obtained in 100% ODE corresponds to tetragonal Zn_3P_2, and the sharpness and high intensity of Bragg reflections suggest the formation of larger crystallites (Figure 3.1). In contrast, the PXRD patterns of NCs synthesized in HDA/ODE exhibit broad humps at 25.8°, 27.0°, 29.2°, 31.3°, 32.3°, 34.2° and 36.9° suggesting the nanoparticulate nature of the reaction product (Figure 3.4). These peaks can be assigned to reflections originating from (211), (202), (212), (220), (203), (301), and (302) crystal planes of tetragonal Zn_3P_2 (JCPDS 01–073–4212). In addition, a high intensity broad reflection corresponding to (400) plane of tetragonal Zn_3P_2 is clearly evident at 44.9°. The broadness of the diffraction patterns is consistent with the Scherrer scattering of small crystallites suggesting that the primary particle size has been significantly reduced in the presence of HDA. The majority of Bragg reflections were not resolved due to combined scattering from crystal planes specifically for NCs prepared at 300 °C for 15–60 min. Nonetheless, the peaks at 27.0°, 31.3°, 34.2°, and 36.9° were resolved with increasing growth time beyond 60 min, consistent with the formation of tetragonal Zn_3P_2. Due to the significant overlap of Bragg reflections in the range of 23°–41°, the average crystallite sizes were calculated by employing the single reflection at 44.9°, which are estimated to be 2.9–5.3 nm for NCs grown at 300 °C for 15–90 min (Table 3.1). The elemental compositions of the Zn_3P_2 crystallites were determined by SEM/EDS and indicate two prominent peaks corresponding to Zn and P with atomic ratios in the range of 56–59% : 44–41% (Figure 3.5), which are consistent with the formation of tetragonal Zn_3P_2.[78]
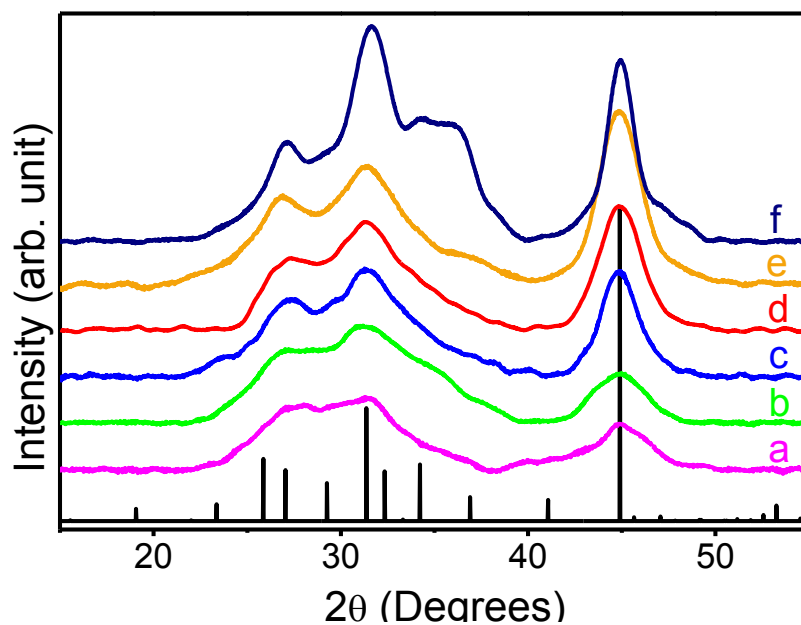
Figure 3.4. Representative powder diffraction patterns of tetragonal Zn_3P_2 NCs synthesized in HDA/ODE at 300 °C for (a) 15, (b) 30, (c) 45, (d) 60, (e) 90, and (f) 180 min. The ICCD–PDF overlay of tetragonal Zn_3P_2 (JCPDS 01–073–4212) is shown as vertical black lines.
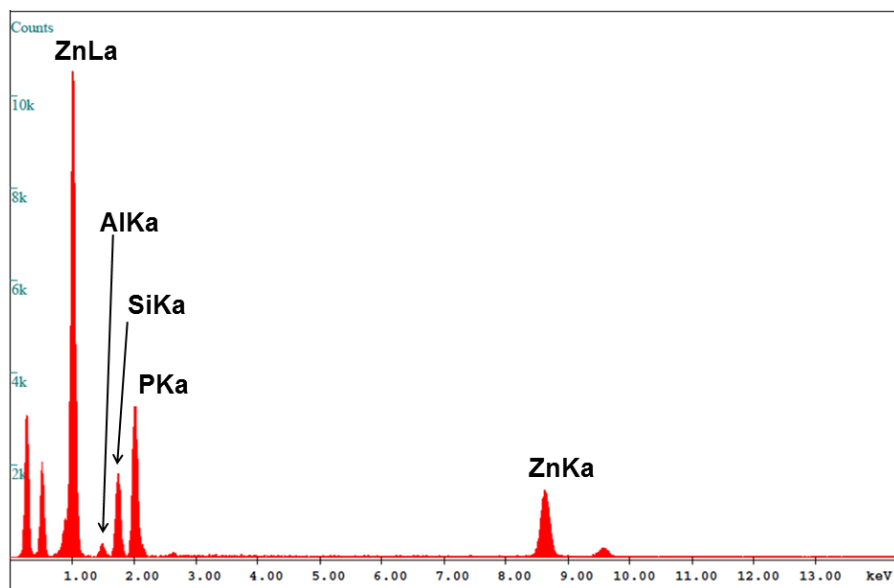
Figure 3.5. A representative SEM/EDS spectrum of the Zn_3P_2 NCs prepared in HDA/ODE at 300 °C for 60 min.

Table 3.1. The absorption band onsets obtained from Kubelka-Munk (KM) and Tauc $((F(KM)hv)^2)$ analyses, PL, PLE data, stoke shifts, full width at half maxima (FWHM), crystallite and average particle size of Zn_3P_2 NCs produced in HDA/ODE at different temperatures and time intervals.

	Crystal size (nm)[a]	Particle size (nm)[b]	Bandgap (KM) (eV)[c]	Bandgap $(F(KM)hv)^2$ (eV)[c]	PL (nm)	PLE (nm)	Stokes Shift (nm)	FWHM (nm)
Zn_3P_2 NCs Grown at 300 °C for different time intervals (min)								
15 min	2.9	4.8 ± 0.7	2.27	2.55	481	345	136	133
30 min	3.8	5.9 ± 0.8	2.15	2.34	504	363	141	161
45 min	4.2	6.6 ± 0.9	1.89	2.09	520	386	134	159
60 min	4.7	8.0 ± 0.7	1.82	2.18	535	396	139	165
90 min	5.3	8.8 ± 1.3	1.68	2.11	545	419	126	176
Zn_3P_2 NCs grown at different nucleation and growth temperatures (°C) for 1 h.								
230 °C	2.0	3.2 ± 0.6	2.51	2.73	469	296	173	143
250 °C	2.3	3.9 ± 0.5	2.37	2.57	491	324	167	112
275 °C	3.7	5.6 ± 0.9	2.28	2.44	511	340	171	152
300 °C	4.7	8.0 ± 0.7	1.82	2.18	535	396	139	165

[a] Average crystallite sizes were calculated by employing the single reflection at 44.9° after applying appropriate correction for instrumental broadening using a Si standard.

[b] Average particle size was calculated from counting 125–150 individual NCs from TEM images.

[c] Optical bandgaps were estimated from extrapolating the linear portion of the absorption profile to the intersection point of the baseline.[87,88,105]

The surface properties of Zn_3P_2 NCs were studied by employing FT–IR, thermogravimetric, and XPS analyses. The characteristic $\nu_{(CHx)}$ (2955, 2916, 2849 cm^{-1}) and ν_{N-H} (3100–3300 cm^{-1}) stretching modes and $\delta_{(CH2)}$ (1465 cm^{-1}) and $\delta_{(N-H)}$ (1590 cm^{-1}) bending modes along with the $\delta_{(CH2)}$ wagging mode (1370 cm^{-1}) observed in NCs synthesized in HDA/ODE suggest the presence of alkyl–amines (Figure 3.6).[106] The presence of bound nitrogen on the NC surface is further evidenced by ν_{N-H} (3145–3286 cm^{-1}) stretches, which were shifted to lower wavenumbers compared to those of free amine (ν_{N-H} = 3165–3336 cm^{-1} for free HDA, Figure 3.6). The observed ν_{N-H} stretches in the NCs were broad and not well resolved which is typical for particles in the nanometer size regime. Additionally, the peaks at 1254 and 2370 cm^{-1} are likely to arise from $\rho_{(Si(CH3)3)}$ and $\nu_{(P-H)}$ vibrational modes of residual $(TMSi)_3P$ surface species.[107] However, the existence of ODE on the surface of the NCs cannot be ruled out, as the $\nu_{(CH2)}$ stretches, which are prominent in the FT–IR spectra, may also be originating from ODE ligands. Moreover, the possible presence of both alkyl–amines and alkenes on the NC surface is suggested by thermogravimetric analyses of the respective NC samples (Figure 3.7).
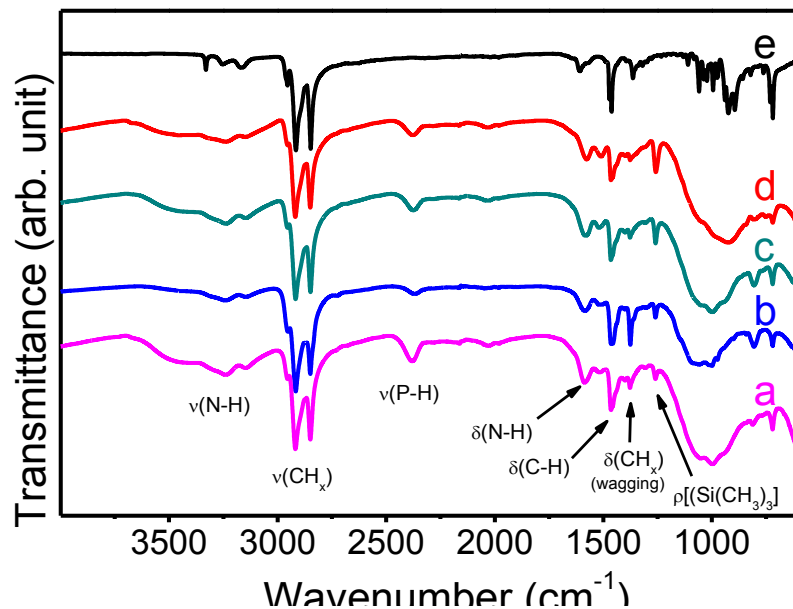
Figure 3.6. FT–IR spectra of Zn_3P_2 NCs synthesized HDA/ODE at 300 °C for (a) 15, (b) 45, (c) 90, and (d) 180 min. along with (e) the FT–IR spectrum of pure HDA.
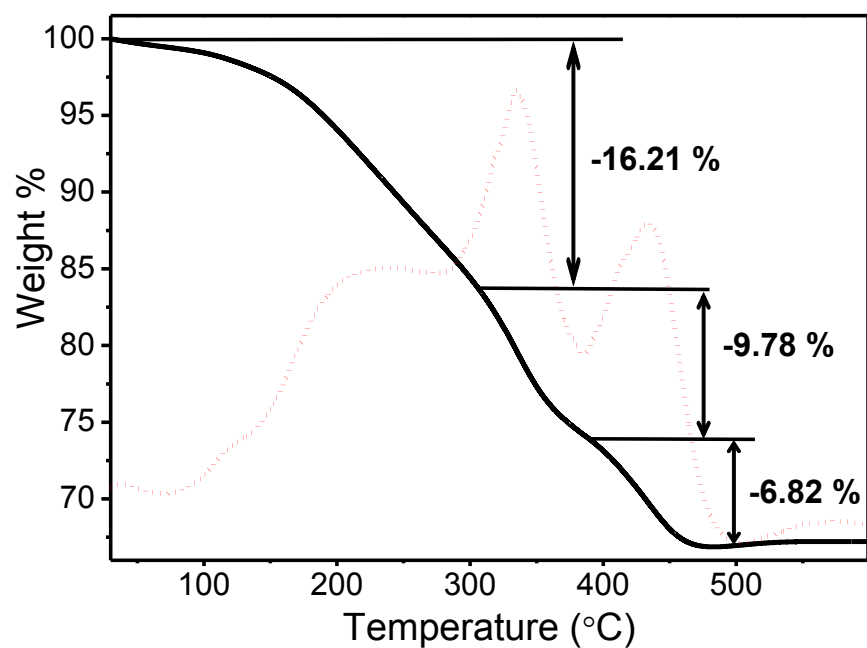
Figure 3.7. A representative TGA plot of the Zn_3P_2 NCs synthesized HDA/ODE at 300 °C for 60 min. Black solid curve illustrates the change in weight % as a function of time, while red dotted line displays the derivative of the previous curve.

A typical TGA curve of the Zn_3P_2 NCs synthesized in HDA/ODE exhibits multistep decomposition leading to the formation of a black residue with a total weight loss of ~32% (Figure 3.7). The derivative curve of the TGA reflects three major desorption events at ~230 °C, ~335 °C and ~430 °C. The first and second weight losses can be attributed to the loss of adsorbed moisture and organic moiety originating from possible $-Si(CH_3)_3$ and ODE surface species (boiling points of $(TMSi)_3P$ and ODE are ~240 and ~315 °C, respectively). The final step can be correlated to the loss of alkyl-amine (HDA), which exhibits a boiling point of ~330 °C. The significantly high temperature (~430 °C) required for alkyl-amine desorption is likely due to strong coordination of HDA to the NC surface, as suggested by XPS (Figure 3.8).[108] The PXRD patterns of the post–annealed TGA residue indicate the presence of tetragonal Zn_3P_2 in all samples (JCPDS 01–073–4212, Figure 3.9). Occasionally, impurity peaks corresponding to hexagonal Zn are observed at $2\theta = 36.1°$, 38.9° and 43.1° in the TGA residue that can be attributed to loss of phosphorus at high temperatures. Consistent with the diffraction data, SEM/EDS analysis of the TGA residue indicates atomic percentages of Zn:P to be 82.3% : 17.7%, further supporting the loss of phosphorus upon thermal decomposition.

The XPS was employed to study the chemical states and surface ligand binding of Zn_3P_2 NCs. The presence of Zn–P bonds are evident in the examination of both P(2p) and $Zn(2p_{3/2})$ binding energies as indicated by a $P(2p_{3/2})$ peak at 128.0 eV[78] in Figure 3.8A and the $Zn(2p_{3/2})$ peak at 1021.4 eV[78] in Figure 3.8B. In addition, further analysis of the P(2p) and $Zn(2P_{3/2})$ regions reveals important information about the state of ligand binding to the NC surface. The presence of HDA has already been confirmed in the FT–IR spectra (Figure 3.6); however FT–IR gives little information on how HDA is

bound to the NC surface. The N(1s) region has a broad peak at 399.8 eV with a full width half maximum of 2.45 eV consistent with multiple states of amine type bonds (Figure 3.8C).[108,109] The less intense peak at 398.1 eV corresponds to N–Zn bonds,[110] and the combination of these peaks is suggestive of a multimodal bonding of N including metal–N complex bonds, in addition to dative bonding and electrostatic interactions.[108] Furthermore, both $Zn(2p_{3/2})$ and P(2p) regions exhibit secondary higher energy peaks at 1023.5 and 132.7 eV, respectively, which can arise from Zn–N and P–N bonds.[111] It has been previously shown that the incorporation of N into ZnO leads to a decrease in $Zn(2p_{3/2})$ binding energy.[109,110] Conversely, in the case presented here, N is more electronegative than P meaning it will pull electrons away from Zn more strongly than P resulting in a higher binding energy for Zn–N bonds than previously reported. To ensure that the Zn(2p) peak at 1023.5 eV is indeed from Zn–N bonds and not from Zn–O bonds, analysis of the O(1s) region is compulsory. Investigation of the O(1s) spectrum in Figure 3.8D reveals only one peak at 532.1 eV, which is consistent with the adsorbed surface O species.[108] There is a clear absence of an Zn–O peak, which would arise between 530.5[108] and 529.0[111] suggesting that the Zn(2p) 1023.5 eV peak arises from Zn–N bonds and not Zn–O bonds. In conjunction with PXRD data, the XPS results support not only the absence of crystalline ZnO but also the amorphous and surface oxidized Zn impurities.
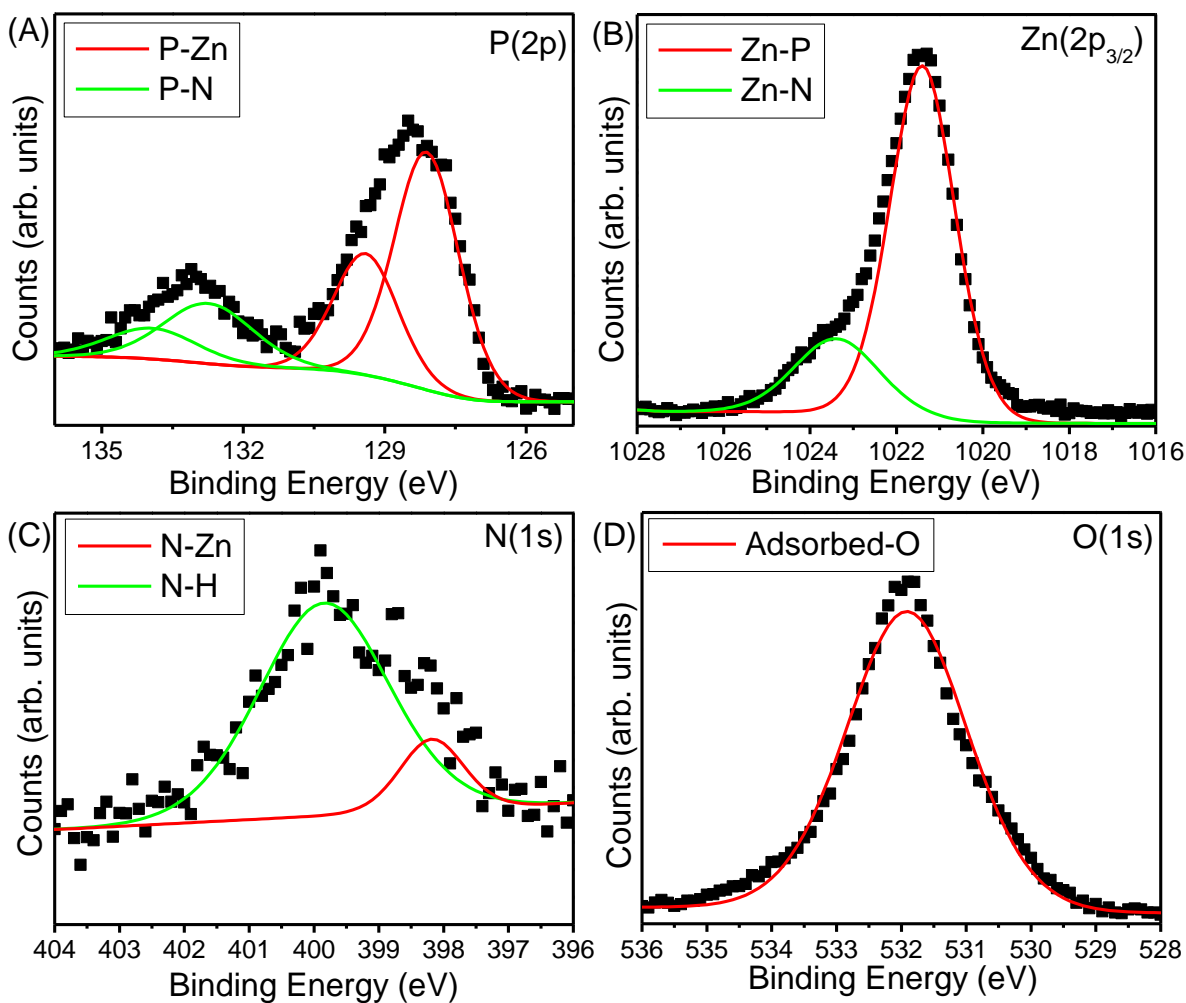
Figure 3.8. Representative XPS spectra of Zn_3P_2 NCs produced in HDA/ODE at 300 °C for 60 min. (A) P(2p) region, (B) $Zn(2p_{3/2})$ region, (C) N(1s) region, and (D) O (1s) region. Dotted lines represent experimental data and solid colored lines correspond to fitted deconvolutions.
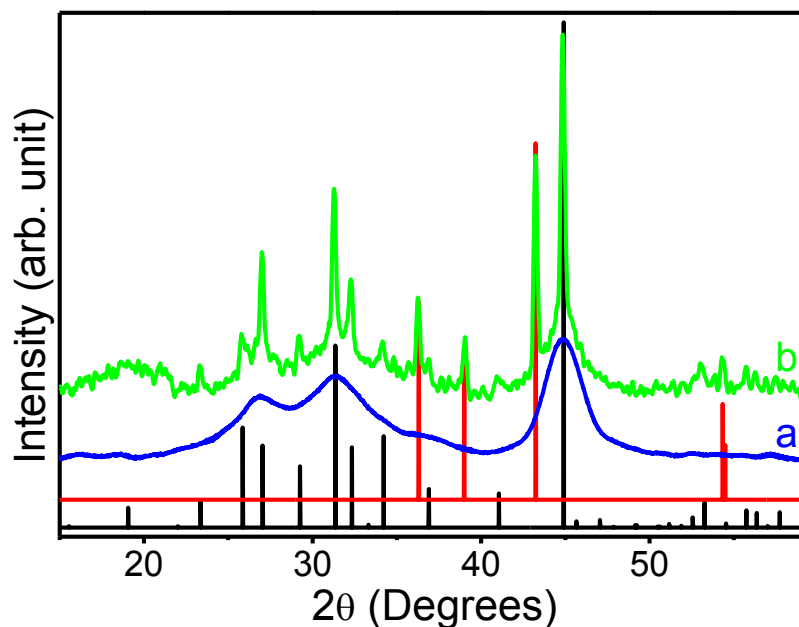
Figure 3.9. PXRD patterns of the (a) Zn_3P_2 NCs prepared at 300 °C for 60 min. along with the (b) post–TGA annealed residue of the sample. The ICCD-PDF overlay of Zn_3P_2 tetragonal (PDF# 01–073–4212) and hexagonal Zn (PDF# 00–004–0831) are shown as vertical black and red lines, respectively.

TEM was employed to investigate the effects of growth time and temperature on morphology and size dispersity of Zn_3P_2 NCs. The alkyl-amine passivated NCs exhibit nearly spherical shape and size dispersity in the range of 11–15 % irrespective of the different growth temperature and reaction times employed in the synthesis (Figure 3.10). TEM images suggest that the NCs produced at shorter growth times (15–30 min.) exhibit narrower size distribution in comparison to those prepared at longer time intervals (45–90 min.). With increasing growth time, the size dispersity of Zn_3P_2 crystallites has slightly increased. This can be attributed to partial Oswald ripening in which the smaller crystallites sacrificially break apart to produce larger and more polydispersed particles.[45] Nonetheless, we have successfully tuned the average particle

size from 4.8 ± 0.7 − 8.8 ± 1.3 nm in HDA/ODE at 300 °C while maintaining the spherical morphology and size dispersity in the range of 11–15 % for as-prepared samples (Figure 3.10A–E). The size dispersity of NCs produced in this study are comparable to recent investigations on highly-quality nonluminescent Zn_3P_2 crystallites reported elsewhere.[101,102] A high-resolution TEM image of an as–prepared NC, which exhibits lattice fringes of 2.01 Å, consistent with the (400) lattice spacing of tetragonal Zn_3P_2,[107] is shown in Figure 3.10C.
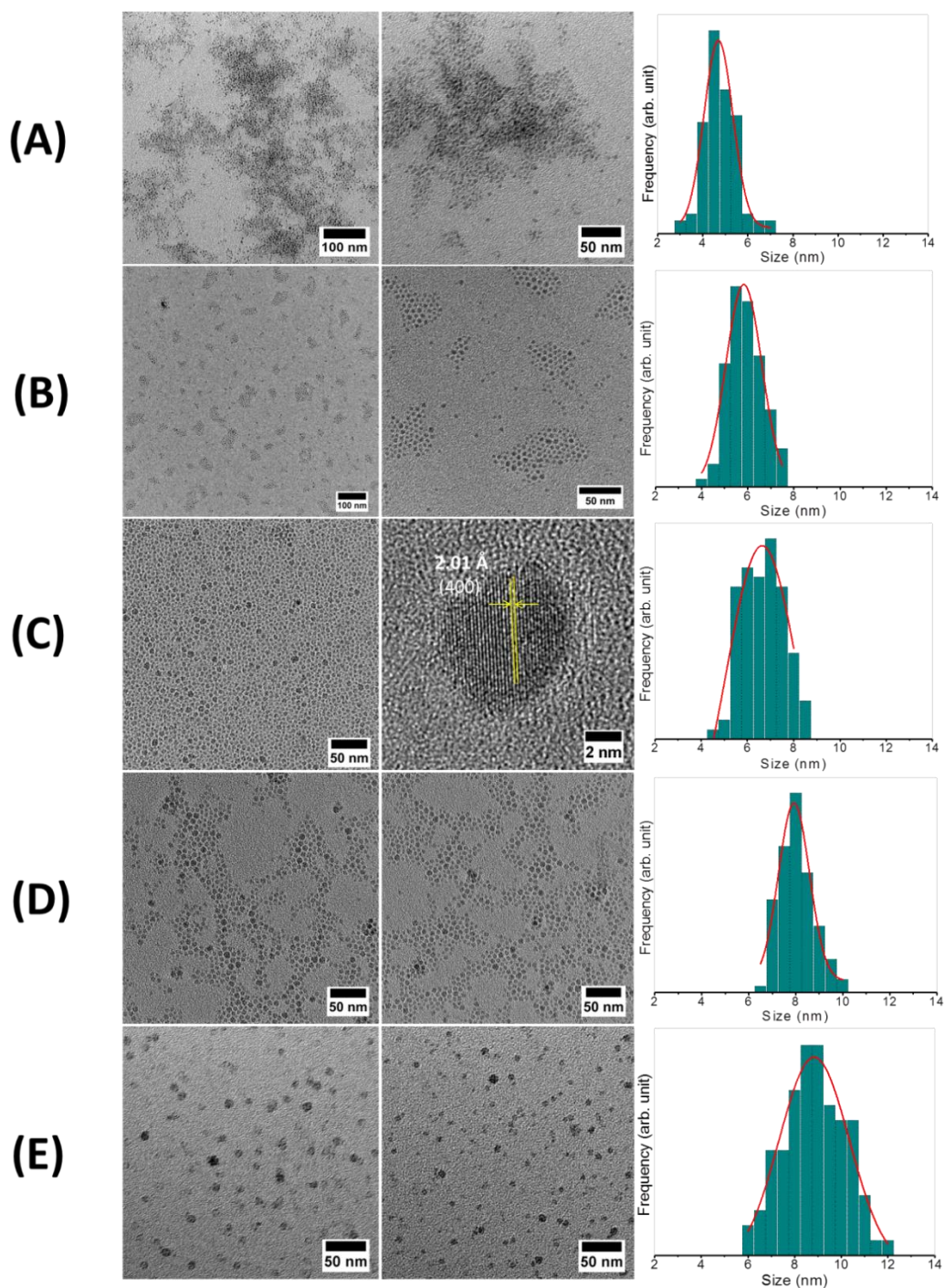
Figure 3.10. TEM images of the Zn_3P_2 NCs prepared in HDA/ODE at 300 °C for (A) 15, (B) 30, (C) 45, (D) 60, and (E) 90 min. The size histograms of Zn_3P_2 NCs without any post synthetic size selection are also shown. The second image in C shows the HRTEM image of a single Zn_3P_2 NC prepared at 300 °C for 45 min.

The optical properties of Zn_3P_2 NCs were investigated using UV-vis-near IR absorption and photoluminescence (PL) studies. The solution absorption spectra (Figure 3.11) exhibit no sharp excitonic features, consistent with the previous reports on Zn_3P_2 NPs.[59] Recently, Glassy et al. reported slightly pronounced excitonic humps for Zn_3P_2 NPs in the size range of 2.6–2.9 nm.[101] The particles reported in that study were significantly smaller and structurally ambiguous in comparison to tetragonal Zn_3P_2 crystallites produced in this study. Hence, the lack of excitonic features can be attributed to either the difference in size or relatively larger dispersity of as-prepared NPs. Further, diffuse reflectance spectroscopy was employed to investigate the absorption band onsets of solid NC samples. Reflectance data were converted to pseudoabsorption using the Kubelka-Munk (KM)[82,88,105] function and the bandgap values were obtained from linear extrapolation of the absorption onsets to the intersection point of the baseline (Figure 3.12, Table 3.1). The bandgap onsets obtained from KM conversion were lower than corresponding emission energies, which is typical for the KM analysis.[82,112] To ascertain more accurate measurements, Tauc plots were employed to account for the nature of energy gaps (direct vs. indirect).[88,113,114] The direct gap Tauc plots of Zn_3P_2 NCs exhibit well-defined absorption onsets that are consistent with the PL energy and systematic red shifts with increasing NC size suggesting size confinement effects (Figure 3.13A–B, Table 3.1). The bandgap onsets of smaller Zn_3P_2 NCs (2.11–2.73 eV, Table 3.1) were significantly blue shifted from those of larger (50–60 nm) crystallites produced in this study (1.45–1.53 eV, Figure 3.2) and the literature reports on bulk tetragonal Zn_3P_2 (1.4–1.5 eV).[59,62] To further investigate the effects of reaction temperature on absorptive properties, temperature-

59

dependent bandgap measurements were performed at different nucleation and growth temperatures (230–300 °C) while the growth time was fixed at 1 h. It was revealed that the absorption onset systematically decreases with increasing growth temperature consistent with the formation of larger crystallites (Figure 3.13B, Table 3.1).
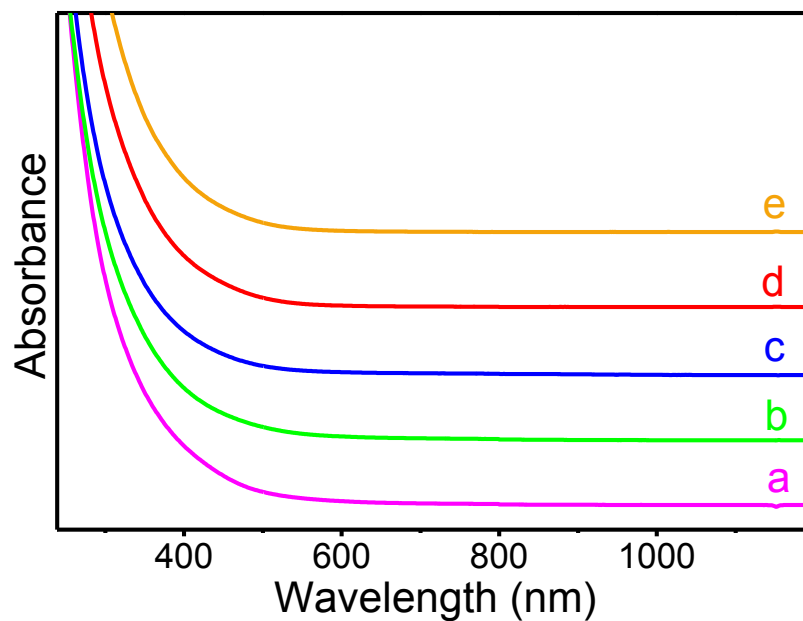
Figure 3.11. Solution absorption spectra of Zn_3P_2 NCs prepared in HDA/ODE at 300 °C for (a) 15, (b) 30, (c) 45, (d) 60, and (e) 90 min.
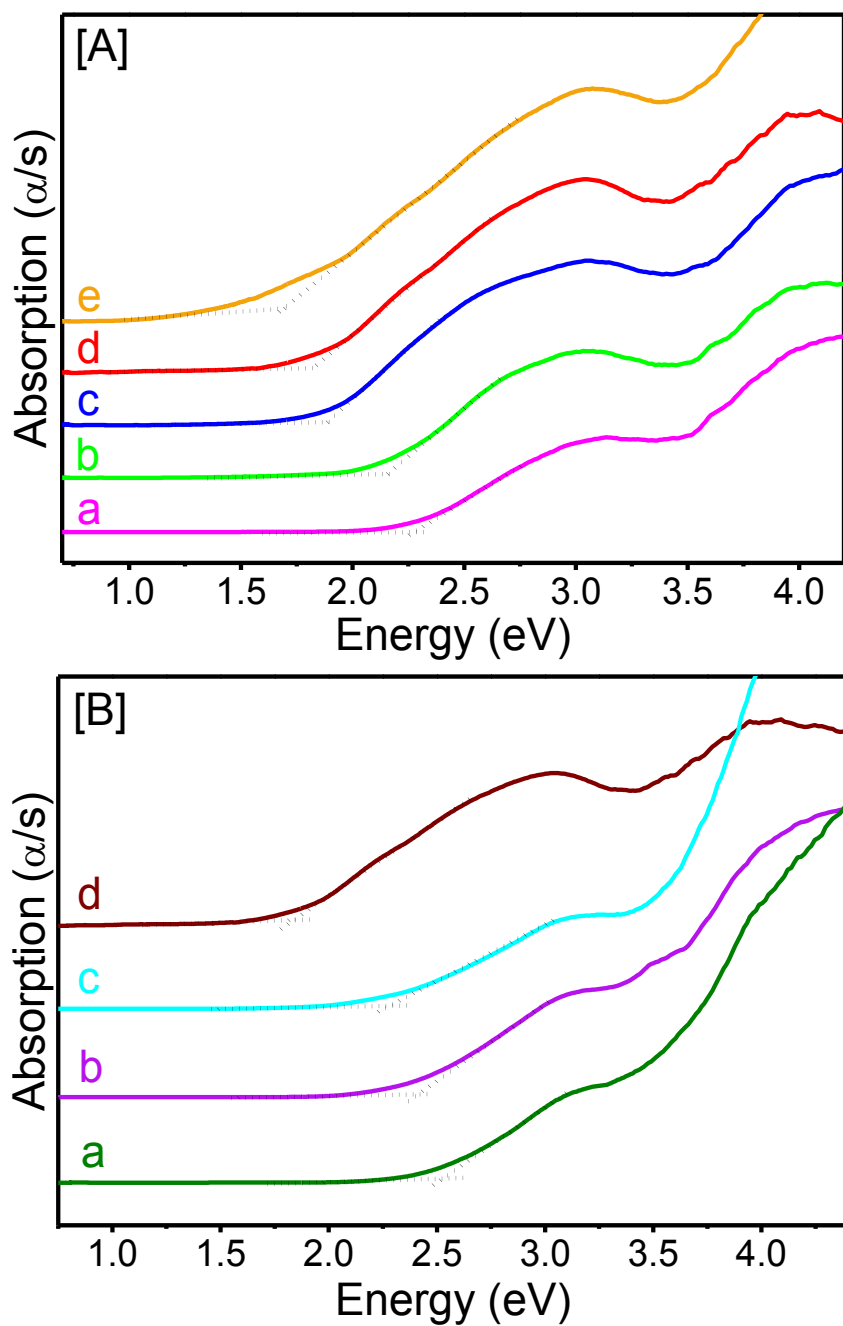
Figure 3.12. Solid–state diffuse reflectance spectra (converted to absorption using Kubelka–Munk function) of [A] Zn_3P_2 NCs synthesized in HDA/ODE at 300 °C for (a) 15, (b) 30, (c) 45, (d) 60, and (e) 90 min. and [B] Zn_3P_2 NCs produced in HDA/ODE at (a) 230 °C, (b) 250 °C, (c) 275 °C, and (d) 300 °C for 1 h.
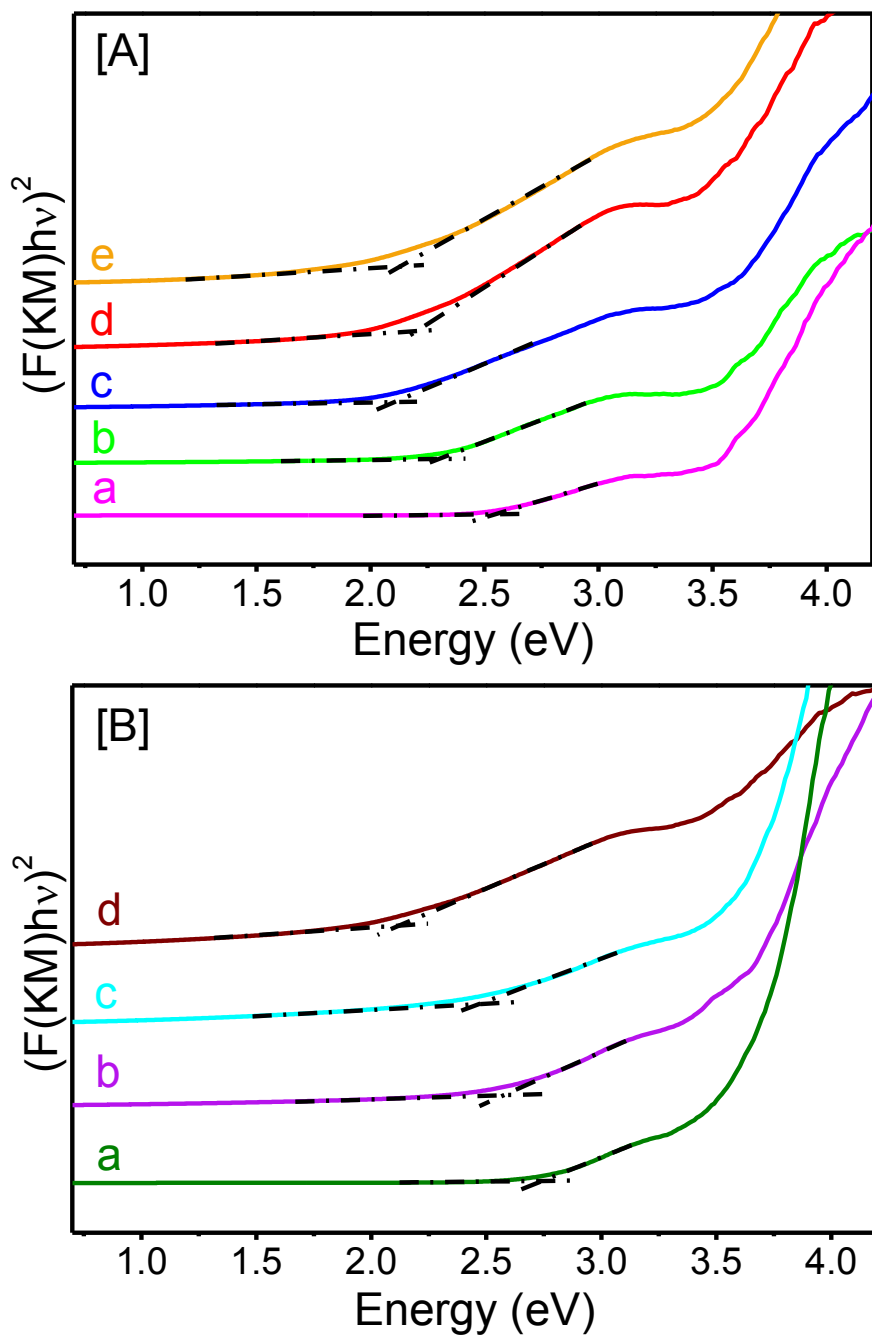
Figure 3.13. Tauc plots of [A] Zn_3P_2 NCs synthesized in HDA/ODE at 300 °C for (a) 15, (b) 30, (c) 45, (d) 60, and (e) 90 min. and [B] Zn_3P_2 NCs produced in HDA/ODE at (a) 230 °C, (b) 250 °C, (c) 275 °C, and (d) 300 °C for 1 h.

The NCs produced at 300 °C for different time intervals exhibit size–tunable emission maxima in the visible spectrum (Figure 3.14A, Table 3.1). PL energy tunability in the range of 481–545 nm was achieved for NCs passivated with HDA ligands. Relatively narrow tunability of emission energies is attributed to the short range of NC sizes (4.8 ± 0.7 – 8.8 ± 1.3 nm) produced in the synthesis. Moreover, a systematic red shift in emission energy and PLE maxima is observed with increasing particle size, consistent with the bandgap data obtained from corresponding NCs (Figure 3.13A, Table 3.1). To confirm the absence of emissive amine impurities, PL spectra of HDA/ODE heated to 300 ºC for 2-3 h were examined (Figure 3.15). HDA exhibits weak emission maxima at ~460 nm with PL QYs of ~0.02 %. In contrast, purified NCs display PL maxima at 481-545 nm with QYs of 0.35–1.6 %, which are typical of related metal phosphide systems.[60,101,115] Further, the emission energy of HDA is not tunable and indicates a broad maxima at ~460 nm, suggesting that the size-tunable luminescence properties are arising from quantum-confined Zn_3P_2 crystallites. Moreover, the time-resolved PL (TRPL) analysis of Zn_3P_2 crystallites yields luminescence lifetimes of 0.6–20.8 ns (Figure 3.16), which are likely to arise from band–edge emission. On the basis of literature reports on II-VI quantum dots, band-edge emission exhibits PL lifetimes of 0.1–5 ns,[116] while emission from surface states is in the range of hundreds of nanosecond to milliseconds.[36,117,118] Therefore, the nanosecond lifetimes obtained for Zn_3P_2 crystallites suggest that the corresponding PL is originating from band-edge luminescence. The mechanism involved with band-edge emission from quantum dots are thoroughly discussed in the literature,[24,36] which accounts for radiative recombination of photogenerated excitons (electron-hole pairs). In cases where

excitation energy exceeds that of the band gap, electrons travel up to higher vibrational levels of the conduction band, resulting in non-radiative relaxation to conduction band edge prior to radiative recombination resulting in Stokes shift in the absorption and emission.[24] Stokes shifts in the range of 126–141 nm (7.4 x 10^5–7.9 x 10^5 cm^{-1}) and full width at half-maximum (fwhm) of 133–176 nm were observed for Zn_3P_2 crystallites grown at 300 °C for different time intervals (15–90 min.). In general, a slight increase in fwhm with increasing growth time is observed, which can be attributed to increasing size dispersity of NCs as suggested by TEM analysis (Figure 3.10). Furthermore, the absence of trap state emission at longer wavelengths[24] is likely due to effective passivation of NCs by alkyl–amines as suggested by FT–IR and XPS analyses.

The temperature-dependent emission spectra of the Zn_3P_2 NCs were also recorded to study the evolution of PL at different nucleation and growth temperatures (Figure 3.14B). This has been performed by producing a series of Zn_3P_2 NCs at 230, 250, 275, and 300 °C for a fixed growth time of 1 h. The corresponding PL spectra exhibit systematic red shifts in emission maxima from 469, 491, 511, and 535 nm, respectively (Figure 3.14B, Table 3.1), which are consistent with the growth of larger crystallites at higher reaction temperatures. In general, a gradual increase in fwhm is observed with increasing growth temperature likely due to increase in size dispersity of particles.
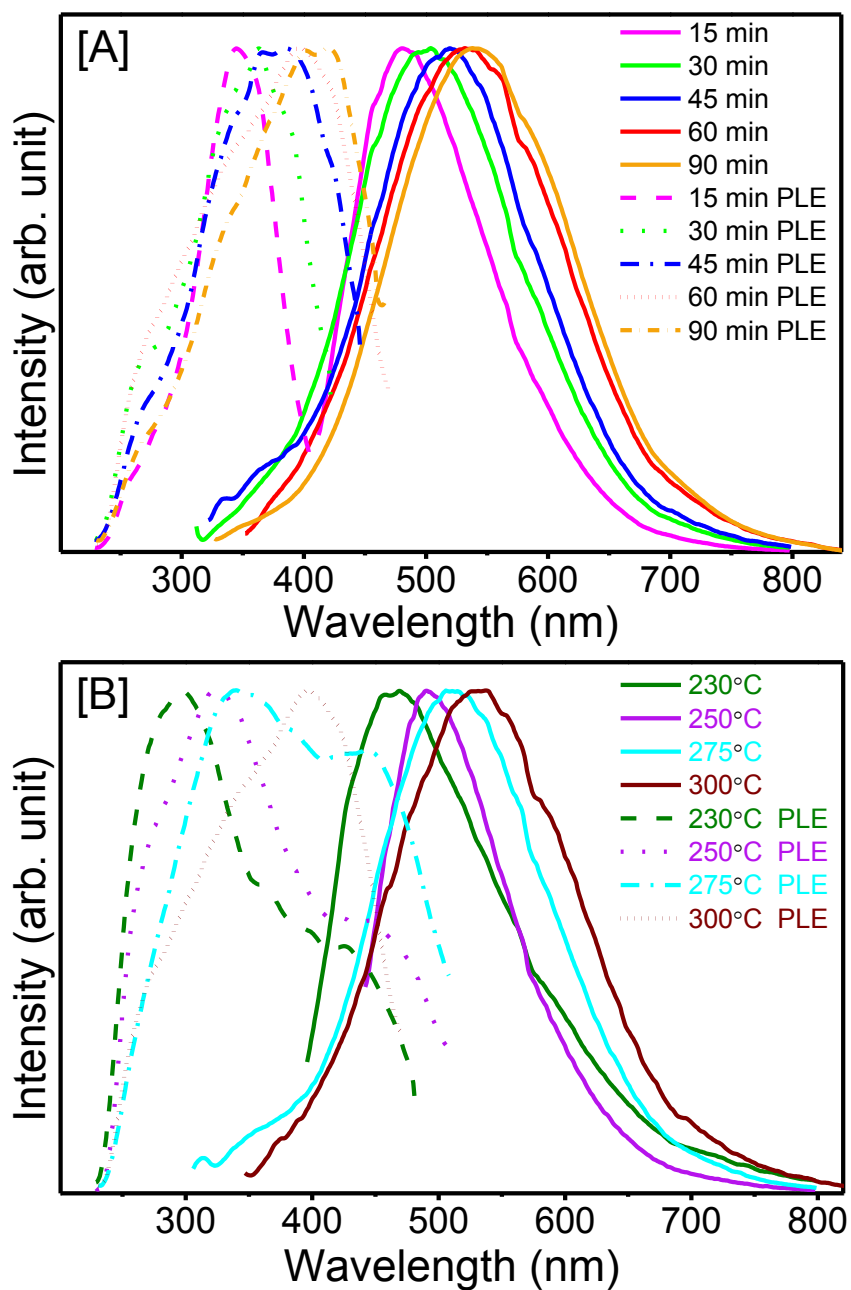
Figure 3.14. PL and PLE spectra of [A] Zn_3P_2 NCs produced in HDA/ODE at 300 °C for 15–90 min. along with the [B] Zn_3P_2 NCs synthesized at different nucleation and growth temperatures (230–300 °C) for a fixed growth time of 1 h.
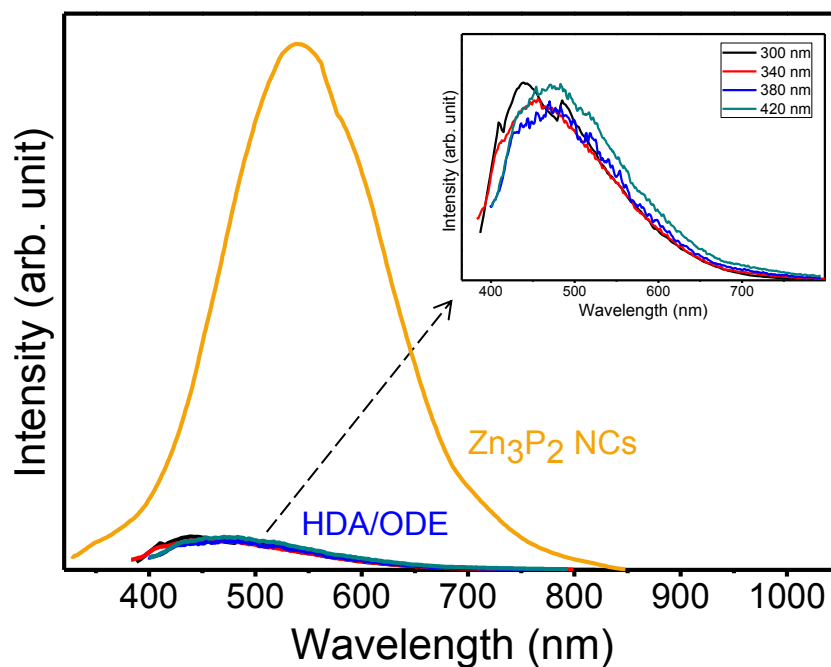
Figure 3.15. Emission spectrum of Zn_3P_2 NCs produced in HDA/ODE at 300 °C for 90 min along with the emission spectra of pure HDA/ODE mixture excited at different wavelengths (300–420 nm). The HDA/ODE mixture was heated at 300 °C for 3 h prior to analysis. Inset shows the magnified plots.
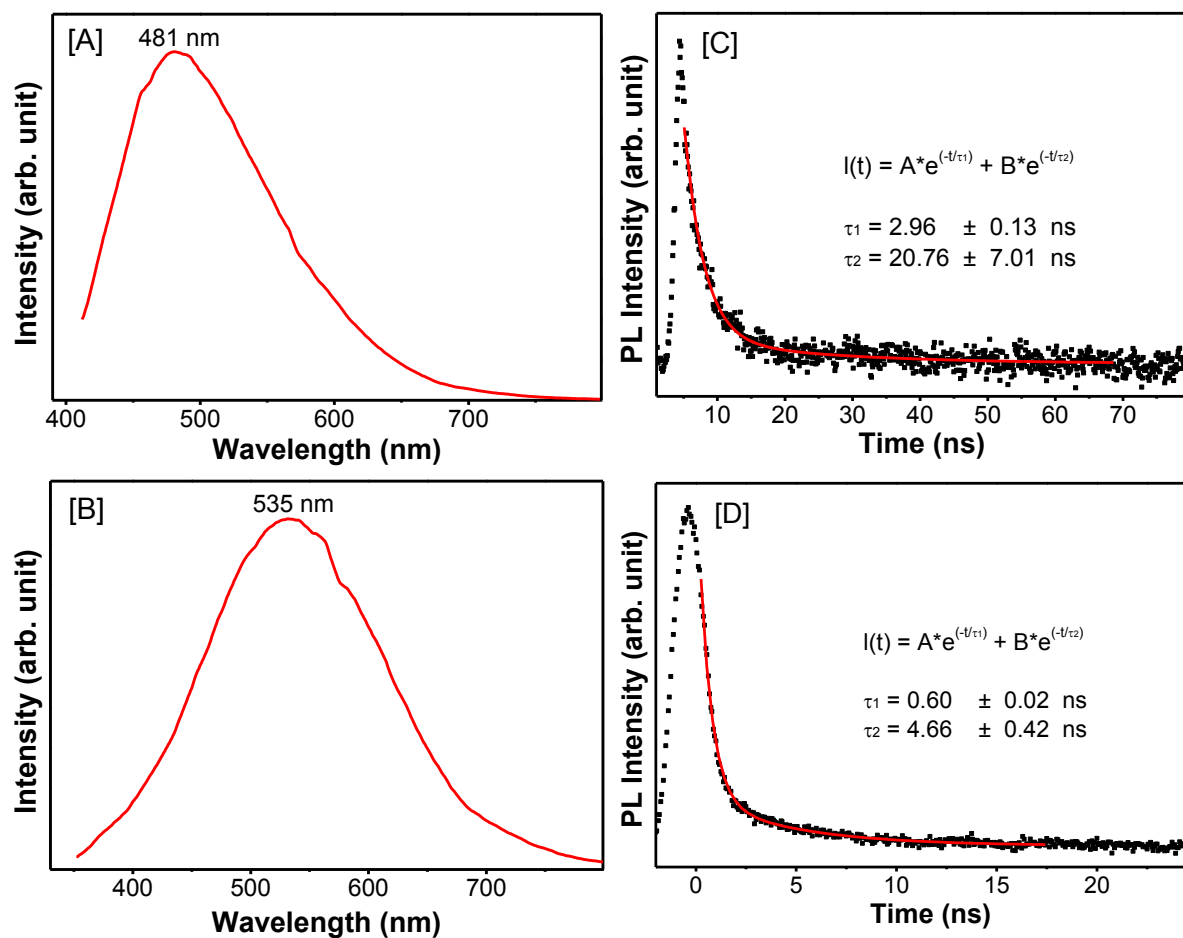
Figure 3.16. Emission spectra of Zn_3P_2 NCs produced in HDA/ODE at 300 °C for [A] 15 min. and [B] 60 min. along with time-resolved photoluminescence plots of corresponding emission: [C] 481 nm and [D] 535 nm.

3.4. Conclusion

We have successfully developed a wet colloidal route for the synthesis of crystalline luminescent Zn_3P_2 NCs by employing $(TMSi)_3P$ and Et_2Zn in high boiling alkene/amine reaction medium. The average particle size has been tuned from 3.2 ± 0.6 to 8.8 ± 1.3 nm by varying the nucleation and growth temperature and the growth time. The absorption onsets estimated for smaller Zn_3P_2 crystallites (2.11–2.73 eV) are

considerably larger than that of bulk Zn_3P_2 (1.4–1.5 eV) suggesting strong quantum confinement effects. As the reaction time or temperature is increased, bandgap decreases, designating the progressive growth of NCs at elevated temperatures. Consistent with the bandgap onsets, PL/PLE maxima indicate a systematic red shift and broadening with increasing growth temperature and time indicating the formation of larger and more polydispersed particles. PL energy tunability from 469 to 545 nm, PLE maxima of 296–419 nm along with 0.35-1.6% luminescent QYs were achieved for tetragonal Zn_3P_2 crystallites passivated with alkyl-amine bonds, N–P and N–Zn, as suggested by FT–IR and XPS analyses. Further studies to expand the PL tunability, narrow the size dispersity, and enhance the emission QYs of Zn_3P_2 NCs will be the future scope of this work. Different capping ligands, surfactant/solvent combinations, and inorganic surface passivation will be investigated for improved synthetic control and to help glean a better understanding of the mechanism involved with the synthesis of Zn_3P_2 NCs.

CHAPTER 4

Colloidal Synthesis and Characterization of Environmental-Friendly Si$_{1-x}$Ge$_x$ Semiconductor Alloy Nanocrystals

4.1. Introduction

Alloyed Si$_{1-x}$Ge$_x$ nanostructures, which represent a class in Group IV semiconductor materials, have received intensive attention due to their potential applications in lithium-ion batteries,[119] bandgap engineering[120], optoelectronic[121] and thermoelectric materials.[122] Since both Ge and Si exhibit indirect bandgap behavior, their use in optics and optoelectronics are not practical. Due to the observed strong luminescence in porous Si produced by chemical etching of bulk silicon,[123] extensive studies have been dedicated to its preparation and optical properties.[124,125] However, unanswered questions remain regarding their emission properties, which were reported to span the visible spectrum. One of the most important issues is the inconsistent reports on the correlation between size and emission color of Si NCs. On the other hand, synthetic efforts on Ge have results in size-dependent luminescence that spans the visible range (350–700 nm)[126] for the inverse micelle technique or the near-IR spectral region (770–1770 nm)[82] for the colloidal technique utilizing strong reducing agents on germanium salts in coordinating solvents. These varying results led to the method of alloying Ge and Si, which is commonly known as bandgap engineering,[127] in order to fine tune the optical energy gap across a wide range of the electromagnetic spectrum by changing

the elemental composition. Production of 5 nm Ge and Si nanoparticles with bandgap values of 1.1 eV[82] and 2.8 eV,[83] respectively from earlier literature reports indicates the need for a robust colloidal synthesis of $Si_{1-x}Ge_x$ alloy nanocrystals with control in size and composition dependent optical properties. The success of this strategy should offer alloyed products for a wide range of application in photovoltaics and photodetection.

4.2.   Experimental

4.2.1. Synthesis of Ge NCs

In a typical experiment, 0.2 g of GeI_2 (0.6 mmol) in 15 mL of dried OLA was placed in a 50 mL three-neck flask attached with a condenser, septum and thermocouple, and 0.9 mL of n-butyllithium (BuLi) in 2 mL of ODE. All these reaction set-ups were done inside a N_2 filled glovebox due to the pyrophoric nature of BuLi and to prevent oxidation of precursors. The GeI_2 in the OLA mixture was allowed to dissolve under vacuum at 120°C for 10–15 min, followed by heating to 230°C under Ar. Upon reaching that temperature, the colorless solution of BuLi/ODE was rapidly injected under fast stirring and continuous Ar flow. The reaction temperature dropped to 178–182°C after the injection, followed by being heated up to 300°C within 3-5 min and kept for 1 hr. The strong reduction power of the BuLi changed the reaction solution from reddish to dark brown. Following the 1 h growth time, reaction flask was cooled down by compressed air, and 10 mL of toluene was added. The resulting NCs were isolated and purified by multi-step redispersion and reprecipitation in toluene and methanol prior to being dried under vacuum for further characterizations.

4.2.2. Synthesis of Si NCs

The colloidal synthesis of Si NCs is carried out similarly to that of Ge NCs, with SiI_4 is used as the precursor rather than GeI_2. A comparable amount of SiI_4 (~0.6 mmol) was added to 15 mL of OLA in a three-neck flask. The Si precursor was mixed well in OLA for 10-15 min, heated to 230°C, reduced by using BuLi and allowed to grow for 1 h at 300°C in a similar fashion to Ge synthesis. After the growth time, the reaction flask was cooled to ~100°C, prior to adding 1 mL of 1-octadecanol for surface coating. As-prepared Si samples were purified by redispersion and reprecipitation in toluene and MeOH inside the glovebox. The resulting Si NCs were kept in an inert atmosphere prior to further characterizations to prevent oxidation.

4.2.3. Synthesis of $Si_{1-x}Ge_x$ NCs

The synthesis of $Si_{1-x}Ge_x$ alloy NCs were carried out in accordance with typical Si synthetic methods. In general, different amounts of GeI_2 and SiI_4 were used according to the desired Ge/Si mole ratio. Figure 4.1 illustrates a typical synthetic route of $Si_{1-x}Ge_x$ alloy NCs.
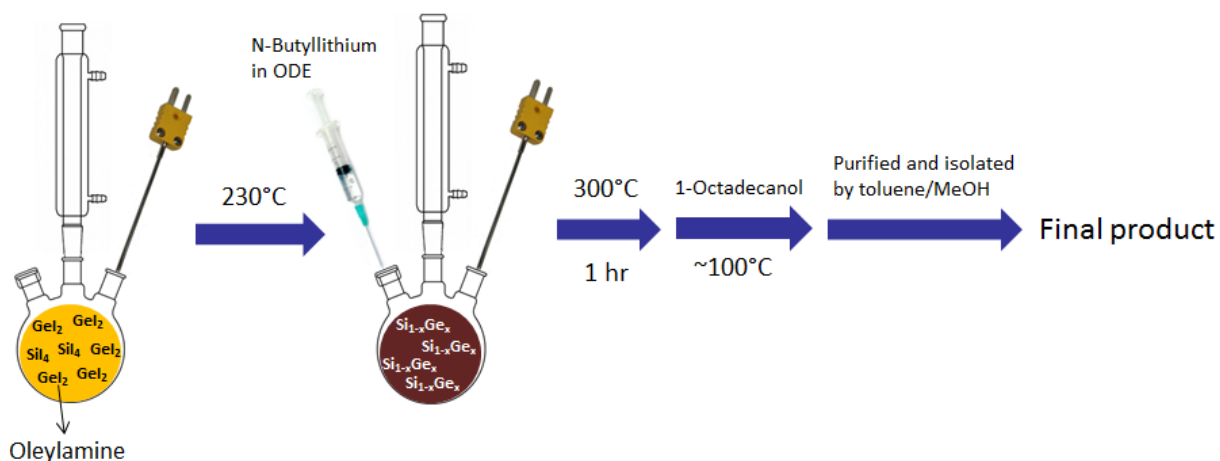
Figure 4.1. A schematic illustration of the colloidal synthesis of $Si_{1-x}Ge_x$ alloy NCs in OLA/ODE.

4.3.   Results and Discussion

4.3.1. Ge NCs

In order to establish the colloidal synthesis of $Si_{1-x}Ge_x$, a single-element Ge synthesis, which was adapted from Ruddy et. al.,[82,128] was carried out confirm the structure and phase purity of the as-prepared products. Accordingly, Ge NCs were produced by the reduction of GeI_2 by BuLi at 300°C in OLA/ODE (surfactant/solvent) solution. PXRD patterns of the as-prepared NCs (Figure 4.2) exhibit diamond-like cubic structure of Ge (JCPDS 01-089-5011). The overall broadness of the Bragg reflections and the overlap of two peaks at 45.3° and 53.6° are evident of the nanoparticulate nature of as-prepared samples. Using the high-intensity reflection at 27.3°, the average crystallite size estimated using Scherrer equation was determined to be 2.6 nm.
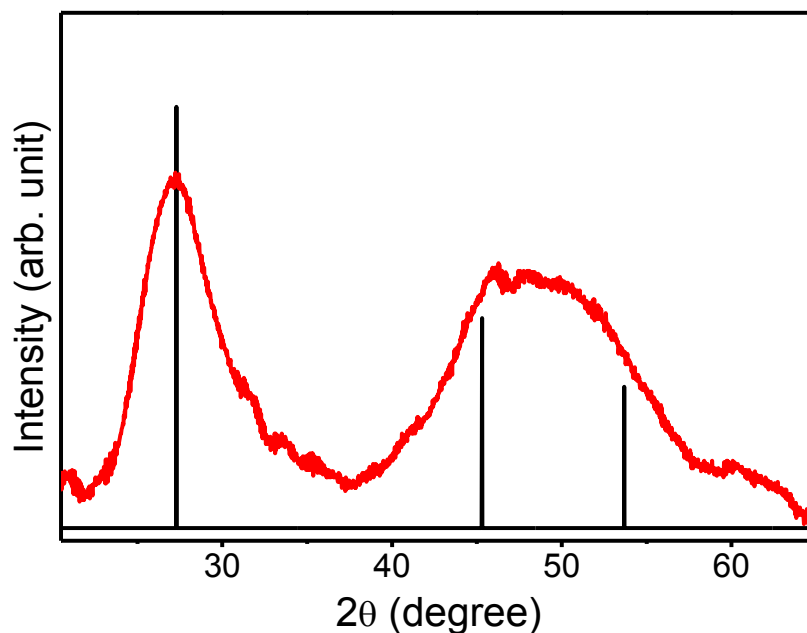
Figure 4.2. PXRD pattern of Ge NCs produced in OLA/ODE at 300°C for 1 h. The diamond-like cubic reference patterns (JCPDS 01-089-5011) are shown as vertical black lines.

In order to confirm the NC formation and gain better understanding of their morphology, TEM was employed to image as-prepared samples dispersed in chloroform. These images confirm the nearly spherical shape of Ge NCs with average size of 3.5 ± 0.6 nm (Figure 4.3A–D). Estimated TEM sizes are slightly higher than that of the crystal sizes determined by Scherrer equation. This difference can be attributed to the surface passivation of the alkyl-amine surfactants present in the reaction mixture.
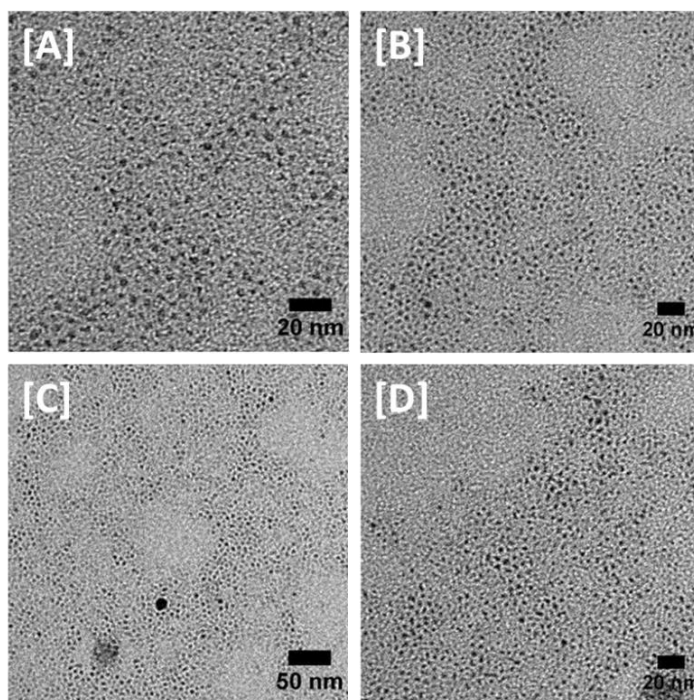
Figure 4.3 Representative TEM images of Ge NCs synthesized in OLA/ODE at 300°C for 1 h.

To investigate the optical properties of Ge NCs, absorption and photoluminescent studies were performed for as-prepared products. There is an absence of an excitonic peak in the solution absorption spectrum (Figure 4.5), which is consistent with the indirect gap nature of Ge. Thus, diffuse reflectance spectroscopy was used to probe the

absorption onsets of solid NC samples. As discussed above for Zn_3P_2 quantum dots, Tauc analysis is usually employed to more precisely determine the bandgap energy of direct or indirect gap materials. The bandgap onset obtained from Tauc plot for indirect-gap (1.28 eV) (Figure 4.4) for nanocrystalline Ge particles were substantially blue shifted from literature reported value for their bulk counterparts (0.67 eV) owing to the size quantum confinement effects.[24,82]
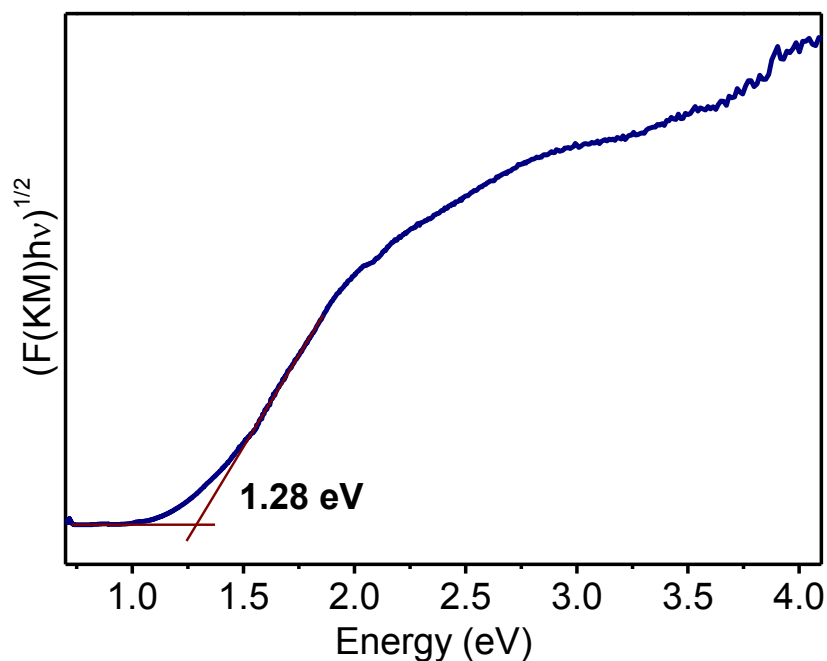
Figure 4.4. A Tauc plot that displays the absorption onset of Ge NCs synthesized in OLA/ODE at 300°C for 1 h.
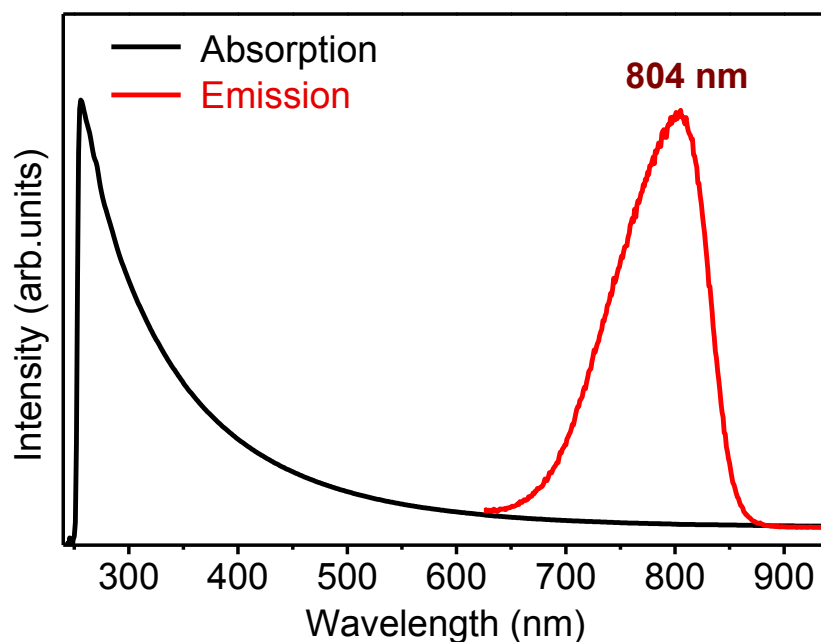
Figure 4.5. Solution absorption and photoluminescence spectra of Ge NCs synthesized in OLA/ODE at 300°C for 1 h.

Despite the absence of an excitonic feature, the emission spectrum exhibits a wavelength maximum at 804 nm (Figure 4.5), which is consistent with earlier report on cubic Ge NCs.[82] Structural, microscopic and optical spectroscopic studies confirmed the quantum confined Ge NCs, with absorption and emission energies blue shifted with respect to the bulk counterpart.

4.3.2. Si NCs

In order to confirm the feasibility of the colloidal synthesis of $Si_{1-x}Ge_x$ alloy NCs, it is important to assure the production of single-element NCs under similar reaction conditions. The synthetic route carried out for Si NPs are the same as that of Ge with the exception of using SiI_4 as the precursor and an additional capping agent (1-

octadecanediol). The structural properties of as-prepared samples performed by PXRD analysis exhibit a featureless pattern, suggesting the amorphous nature of resulting Si NPs (Figure 4.6), consistent with the literature reports for colloidal NPs.[83] The amorphous structure of the NP product is also evidenced by the oiliness of the sample, which cannot be purified completely.
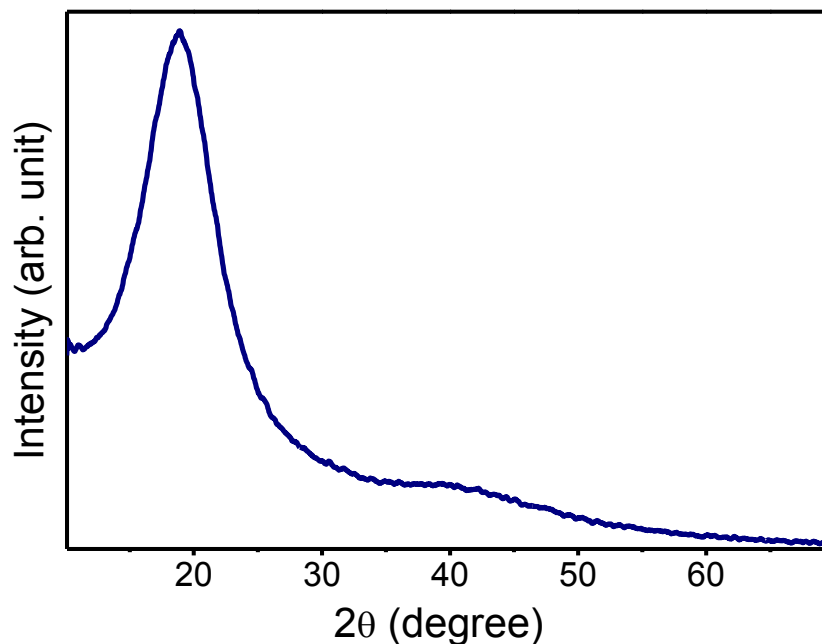
Figure 4.6. PXRD patterns showing the amorphous nature of Si NPs synthesized in OLA/ODE at 300°C for 1 h.

TEM studies carried out for Si samples dispersed in chloroform reveal quasi-spherical morphology of as-prepared NPs (Figure 4.7A–C). An average size of 4.9 nm with standard deviation of distribution comes in the range of 13–17% were obtained for colloidal Si NPs. The analyzed TEM images display a degree of residual surfactants retained around the particles, indicating an incomplete purification of the alkyl amines that cause the oily behavior of the samples.
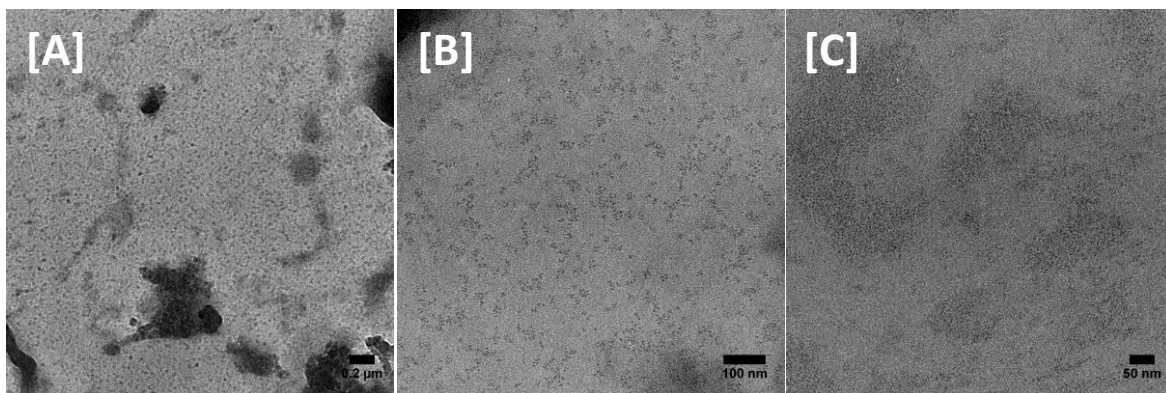
Figure 4.7. Representative TEM images of Si NPs synthesized in OLA/ODE at 300°C for 1 h.

Similar to Ge, Si is an indirect-gap material, thus the solution absorption spectrum shows no sign of an excitonic feature. According to previous studies, wet chemical synthesis, usually yield blue emission for luminescent Si NCs. Photoluminescence spectra of as-prepared Si NPs exhibited wavelength maxima in the near UV region of 380 nm (Figure 4.8), similar to earlier investigations, and greatly blue-shifted with respect to emission of Ge NCs obtained above. This gives rise to the composition-dependent emission tunability of $Si_{1-x}Ge_x$ alloy NCs from the UV to visible spectrum. In addition, solid-state absorption performed by employing diffuse reflectance spectroscopy exhibit a bandgap onset of ~3.11 eV (Figure 4.9), consistent with the emission energy. This significant blue shift in band energy with respect to the macrocrystalline bulk form of Si (1.12 eV) emphasizes quantum confinement effects in Si NPs.
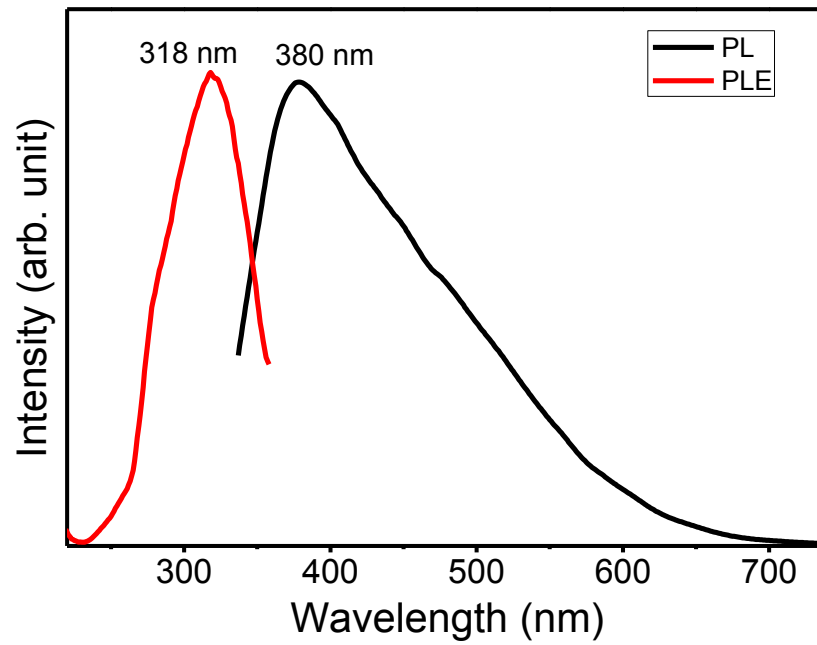
Figure 4.8. PL and PLE spectra of Si NPs synthesized in OLA/ODE at 300°C for 1 h.
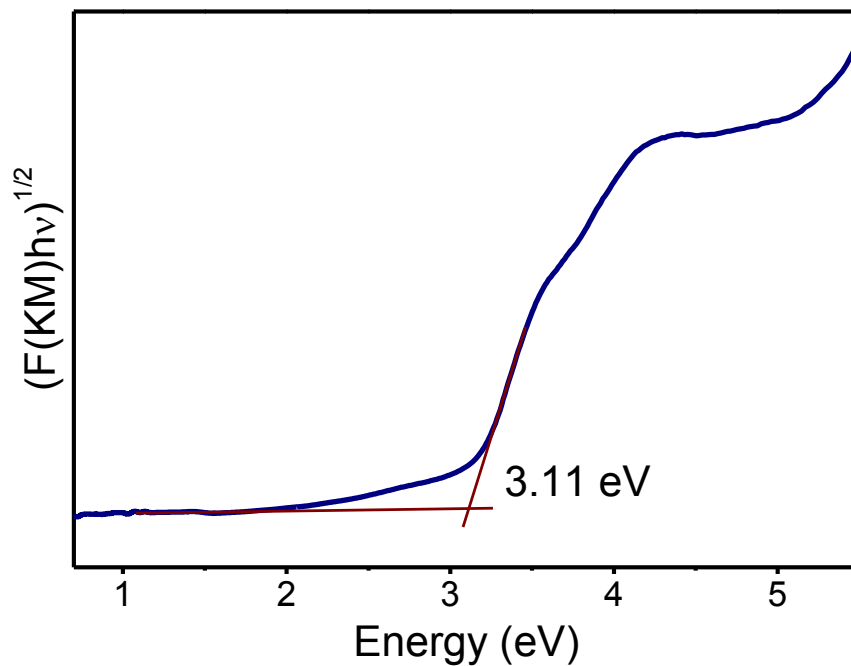
Figure 4.9. A Tauc plot illustrating the absorption onset of Si NPs synthesized in OLA/ODE at 300 °C for 1 h.

4.3.3. Si$_{1-x}$Ge$_x$ NCs

The success in wet-colloidal production of elemental Ge and Si NCs employing similar synthetic conditions inspires the creation of their alloyed NCs, providing more options for new material design of nanoparticles while retaining the novel properties of individual compound material. One of the key factors influencing the fabrication of homogeneous alloys is the comparability in reaction conditions, and the growth process of one component material must not impede that of the other. In addition, their structural comparability should be able to smoothly facilitate the mixing to prevent the formation of unwanted structural impurities. The high miscibility, similar electronic valency and low lattice mismatch between Ge and Si highly favors their homogeneous alloying. Besides, the use of highly coordinating solvent mixtures (OLA/ODE) at moderately high temperatures (~230°C) can sufficiently solvate Ge and Si precursors, thus easing the co-nucleation and growth of nanoalloys. Due to the successful fabrication of nanocrystalline Ge particles and the amorphous nature of resulting Si NPs, alloying effects with a low amount of Si should create substitutions of Si atoms into Ge lattice structure, which can potentially maintain the crystallinity of Ge in the alloyed products.

Experimentally, Si$_{1-x}$Ge$_x$ NCs with compositions in the range of x = 82.1–92.5 were produced by co-reduction of GeI$_2$ and SiI$_4$ at 230 °C, followed by the growth of small nuclei at 300 °C for 1 h. In order to confirm the homogeneous alloying of Ge and Si, PXRD was used to probe the change in crystal structure and the presence of any impurities of the solid product. Silicon has smaller atomic radius than Ge does, thus incorporation of Si atom into Ge crystal structure will cause shrinkage in its lattice,

shifting the Bragg reflections to higher 2θ. Figure 4.10 displays the PXRD patterns of $Si_{1-x}Ge_x$ alloy NCs with different elemental compositions.
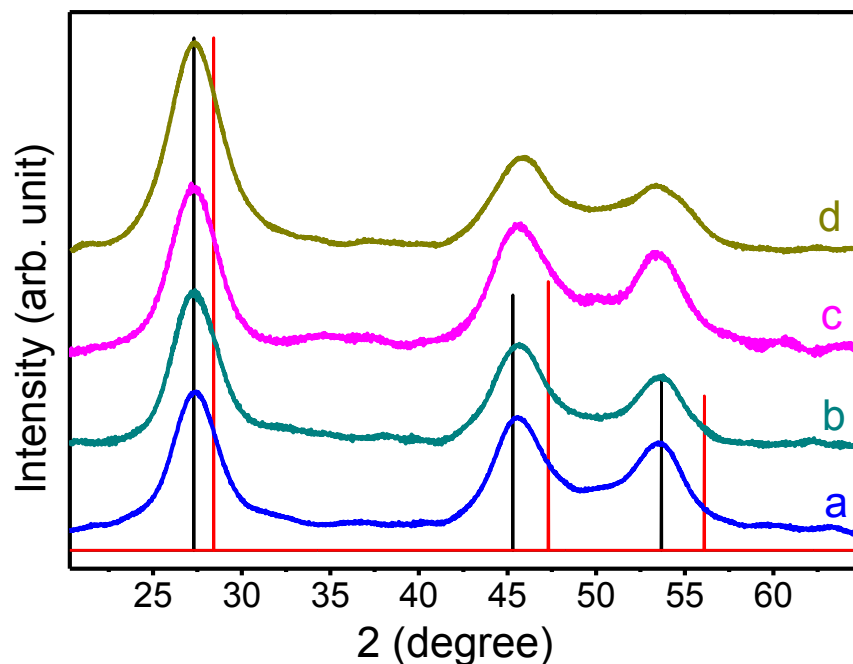
Figure 4.10. Powder diffraction patterns of cubic $Si_{1-x}Ge_x$ NCs, where (a) x = 82.1, (b) x = 87.5, (c) x = 88.2, and (d) = 92.5, prepared in OLA/ODE at 300 °C for 1 h. The cubic reference patterns for Ge (JCPDS 01-089-5011) and Si (JCPDS 01-072-1088) are shown as vertical black and red lines, respectively.

From the PXRD patterns of as-prepared samples, it shows that the efficient reduction of Ge salts and the crystallization of Ge NCs were achieved. It also illustrates that the diamond-like cubic structure of Ge is maintained regardless of the amount of Si precursor added into the reaction. Although SEM/EDS analysis confirmed the presence of both Ge and Si in $Si_{1-x}Ge_x$ NC samples, PXRD patterns exhibit no significant shift in Bragg reflections, suggesting there is insufficient evidence for the incorporation of Si into Ge lattice structure, which is a requirement for homogeneous alloying.

In order to investigate the optical tunability of $Si_{1-x}Ge_x$ alloy NCs as a result of alloying and quantum confinement effect, absorption and photoluminescence spectroscopy was employed to probe these properties. Similar to pure Ge and Si, there is still an absence of an excitonic feature for $Si_{1-x}Ge_x$ alloy NCs, which clearly confirms their indirect gap nature. With bandgap absorption onset of 1.28 eV and 3.1 eV obtained for Ge and Si NCs, respectively, tunable onset values intermediate to 1.28 and 3.1 are expected for resulting $Si_{1-x}Ge_x$ NCs. However, Figure 4.11 indicates that there is insignificant change in absorption onsets with changing Ge compositions from 82.1% to 92.5% in $Si_{1-x}Ge_x$ products. These slight fluctuations in the range of 0.98–1.04 eV for the bandgap onsets could be due to the poor spectral resolution or the difference in concentration of solid samples used for the analysis.
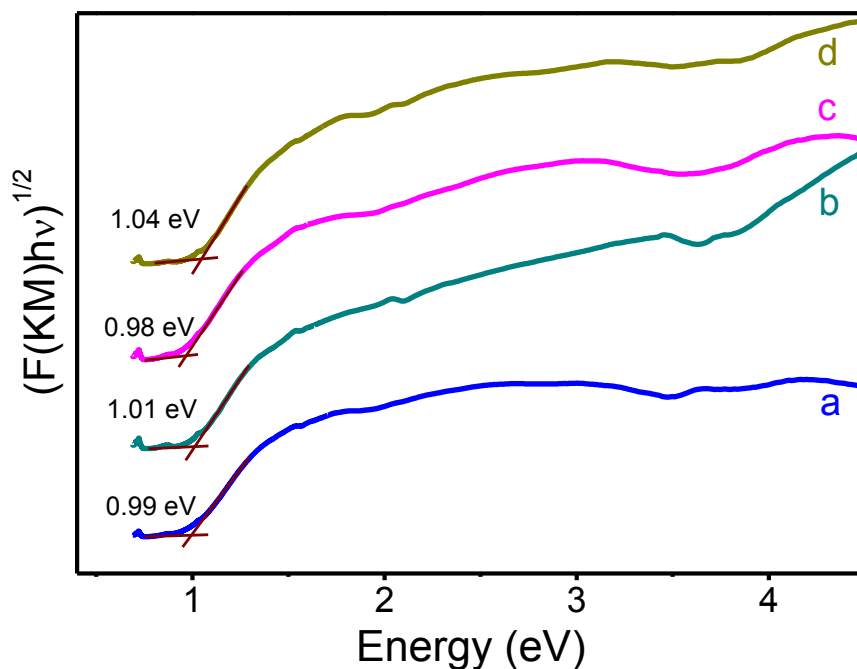
Figure 4.11. Tauc plots showing the absorption onsets of $Si_{1-x}Ge_x$ NCs with different elemental compositions. (a) x = 82.1, (b) x = 87.5, (c) x = 88.2, and (d) = 92.5.

Nonetheless, these energy gap values are blue shifted with respect to the bulk Ge, thus strongly indicate the formation of Ge NCs, which are also confirmed by their PXRD patterns. With the observed structural and optical characterizations, there is no evidence showing the incorporation of Si into Ge crystal structure, hence homogeneous alloys of Ge and Si are not achieved. This phenomenon could be attributed to the much higher surface energy of Ge nuclei, which only favors the crystallization of Ge NCs in solution, prohibiting the contribution of Si. In order to overcome this challenge, additional use of a crystallization agent is need to facilitate the nucleation and growth of Si NCs. Schaak and coworkers were able to use HMDS as a crystallization agent in production of highly crystalline and monodispersed Ge NPs without using strong reducing agent like n-BuLi or LiAlH$_4$.[129] Moreover, the use of different surfactants and solvents can also improve the nucleation and growth kinetics of Si, thus promoting the simultaneous crystallization of Ge and Si.

4.4.   Conclusion

We have attempted to develop a colloidal synthesis of Si$_{1-x}$Ge$_x$ alloys NCs via co-reduction of GeI$_2$ and SiI$_4$ in OLA/ODE surfactant/solvent mixtures at moderately high temperature (230–300 °C). Single-element Ge NCs were successfully produced via a wet chemical method adapted from literature. The resulting Ge nanocrystalline particles exhibit diamond-like cubic structure with nearly spherical morphology with an average size of 3.5 ± 0.6 nm. Optical absorption and emission spectroscopic studies indicate blue shifts in the bandgap onset and photoluminescence with respect to bulk Ge. In contrast with the crystallinity of Ge NCs, Si NPs prepared under similar synthetic

conditions result in amorphous particles, but their optical properties still show size confinement effects. Due to structural comparability of Ge and Si, this colloidal route was used to fabricate $Si_{1-x}Ge_x$ alloy NCs with composition-dependent optical properties. Powder X-ray diffraction and solid-state absorption spectroscopic studies reveal the inability of Si to be incorporated into Ge structure, owing to the large difference in crystallization temperatures of the two materials. The successful outcome of this synthesis for $Si_{1-x}Ge_x$ nanoalloys will demand the use of crystallization agent or different surfactant/solvent medium to facilitate the simultaneous nucleation and growth of Ge and Si.

SUMMARY

Successful colloidal synthesis of luminescent Zn_3P_2 quantum dots were done via hot injection of highly reactive $(TMSi)_3P$ and Et_2Zn in a high boiling surfactant/solvent (hexadecylamine/octadecene) mixture. The development of this synthetic strategy stems from the natural abundance and low toxicity of Zn_3P_2 material along with its direct gap energy that is ideal for solar energy absorption. Wet-colloidal syntheses have proven be the most favorable approach for fabrication of high quality quantum dots in various sizes and shapes owing to their ability to have high control over nucleation and growth kinetics of the nanocrystals. The resulting Zn_3P_2 NCs with average sizes of 3.2–8.8 nm were observed to exhibit exceptional size-dependent absorption and emission properties. The small size particles exhibit high quantum confinement effects, with absorption onsets blue shifted to much larger values (2.11–2.73 eV) compared to the ones observed for the bulk Zn_3P_2 (1.4–1.5 eV). Size tunability was done by varying the time or temperature associated with the nucleation and growth processes. The synthesis indicated a direct relationship between particle size and reaction time or temperature. Bandgap onsets and emission maxima also show systemic blue shifts with reduction of particle sizes, indicating optical tunability as a function of size, consistent with size confinement effects. Relatively low quantum yields (0.35–1.6%) were estimated for these alkyl-amine capped Zn_3P_2 quantum dots, thus its improvement will be the scope of future work for this system.

Efforts to produce a new class of colloidal $Si_{1-x}Ge_x$ alloy NCs were done via simultaneous reduction of Ge and Si salts in a coordinating solvent at elevated temperatures. Although the synthetic route was adopted from literature, different reaction parameters were fine-tuned to achieve successful alloying of the two materials on the nanoscale. Ge and Si were first prepared individually and showed successful production of cubic crystalline Ge NPs, while the resulting Si NPs remain amorphous. Due to the high structural comparability and large bandgap difference of Ge and Si NPs, their alloyed form was designed to take advantage of the composition-dependent optical tunability. As prepared Ge NCs exhibit quasi-spherical morphology with average size of ~3.5 nm and bandgap onset of 1.28 eV, which is highly blue shifted from the bulk value (0.67 eV), consistent with the size confinement effect. With the absorption onset estimated at 3.11 eV for synthesized Si NPs, bandgap engineering through alloying in the nanoscale will enable the optical tunability across the visible to near IR region for $Si_{1-x}Ge_x$ nanoalloys by changing their elemental compositions. However, as-prepared $Si_{1-x}Ge_x$ nanoalloys display no tunable absorption and no Si incorporation into the cubic Ge crystal structure according to diffuse reflectance spectroscopic and PXRD characterizations. This phenomenon is attributed to the early nucleation and crystallization of Ge in comparison to Si. Therefore, the scope of future work for this system is to investigate different ligands that can be used as crystallization agents to help in facilitating the nucleation of and growth of Si NPs to be comparable with Ge.

REFERENCES

(1)   Wilcoxon, J. P.; Samara, G. A. *Appl. Phys. Lett.* **1999**, *74*, 3164–3166.

(2)   Murray, C. B.; Norris, D. J.; Bawendi, M. G. *J. Am. Chem. Soc.* **1993**, *115*, 8706–8715.

(3)   Eckhoff, D. A.; Sutin, J. D. B.; Clegg, R. M.; Gratton, E.; Rogozhina, E. V.; Braun, P. V. *J. Phys. Chem. B* **2005**, *109*, 19786–19797.

(4)   Keating, C. D.; Musick, M. D.; Keefe, M. H.; Natan, M. J. *J. Chem. Educ.* **1999**, *76*, 949–955.

(5)   Song, Q.; Zhang, Z. J. *J. Am. Chem. Soc.* **2004**, *126*, 6164–6168.

(6)   Osuna, J.; de Caro, D.; Amiens, C.; Chaudret, B.; Snoeck, E.; Respaud, M.; Broto, J.-M.; Fert, A. *J. Phys. Chem.* **1996**, *100*, 14571–14574.

(7)   Colvin, V. L.; Schlamp, M. C.; Alivisatos, A. P. *Nature* **1994**, *370*, 354–357.

(8)   O'Regan, B.; Gratzel, M. *Nature* **1991**, *353*, 737–740.

(9)   Inasawa, S.; Sugiyama, M.; Yamaguchi, Y. *J. Phys. Chem. B* **2005**, *109*, 3104–3111.

(10)   Li, Z. F.; Swihart, M. T.; Ruckenstein, E. *Langmuir* **2004**, *20,* 1963–1971.

(11)   Puntes, V. F.; Krishnan, K. M.; Alivisatos, A. P. *Science* **2001**, *291*, 2115–2117.

(12)   Wang, H.; Northwood, D. O. *J. Mater. Sci.* **2008**, *43*, 1050–1056.

(13)   Ely, T. O.; Pan, C.; Amiens, C.; Chaudret, B.; Dassenoy, F.; Lecante, P.; Casanove, M.-J.; Mosset, A.; Respaud, M.; Broto, J.-M. *J. Phys. Chem. B* **2000**, *104*, 695–702.

(14)   Sun, S.; Murray, C. B.; Weller, D.; Folks, L.; Moser, A. *Science* **2000**, *287*, 1989–1992.

(15)   Perera, S. C.; Tsoi, G.; Wenger, L. E.; Brock, S. L. *J. Am. Chem. Soc.* **2003**, *125*, 13960–13961.

(16)   Perera, S. C.; Fodor, P. S.; Tsoi, G. M.; Wenger, L. E.; Brock, S. L. *Chem. Mater.* **2003**, *15*, 4034–4038.

(17)   Poizot, P.; Laruelle, S.; Grugeon, S.; Dupont, L.; Tarascon, J. M. *Nature* **2000**, *407*, 496–499.

(18)   Son, S. J.; Reichel, J.; He, B.; Schuchman, M.; Lee, S. B. *J. Am. Chem. Soc.* **2005**, *127*, 7316–7317.

(19)   Tanase, M.; Bauer, L. A.; Hultgren, A.; Silevitch, D. M.; Sun, L.; Reich, D. H.; Searson, P. C.; Meyer, G. J. *Nano Letters* **2001**, *1*, 155–158.

(20)   Schulz, J.; Roucoux, A.; Patin, H. *Chem.-Eur. J.* **2000**, *6*, 618–624.

(21)   Collier, P. J.; Iggo, J. A.; Whyman, R. *J. Mol. Catal. A-Chem.* **1999**, *146*, 149–157.

(22)   Senevirathne, K.; Burns, A. W.; Bussell, M. E.; Brock, S. L. *Adv. Funct. Mater.* **2007**, *17*, 3933–3939.

(23)   Dhas, N. A.; Suslick, K. S. *J. Am. Chem. Soc.* **2005**, *127*, 2368–2369.

(24)   Trindade, T.; O'Brien, P.; Pickett, N. L. *Chem. Mater.* **2001**, *13*, 3843–3858.

(25)   Smith, A. M.; Nie, S. *Acc. Chem. Res.* **2010**, *43*, 190–200.

(26)   Elliott, R. J. *Phys. Rev.* **1957**, *108*, 1384–1389.

(27)   Vossmeyer, T.; Katsikas, L.; Giersig, M.; Popovic, I. G.; Diesner, K.; Chemseddine, A.; Eychmueller, A.; Weller, H. *J. Phys. Chem.* **1994**, *98*, 7665–7673.

(28)   Goldstein, A. N.; Echer, C. M.; Alivisatos, A. P. *Science* **1992**, *256*, 1425–1427.

(29)   Tolbert, S. H.; Alivisatos, A. P. *Annu. Rev. Phys. Chem.* **1995**, *46*, 595–626.

(30)   Pickett, N. L.; O'Brien, P. *Chem. Rec.* **2001**, *1*, 467–479.

(31)   Alivisatos, A. P. *Science* **1996**, *271*, 933–937.

(32)   Robel, I.; Subramanian, V.; Kuno, M.; Kamat, P. V. *J. Am. Chem. Soc.* **2006**, *128*, 2385–2393.

(33)   Strauf, S.; Hennessy, K.; Rakher, M. T.; Choi, Y. S.; Badolato, A.; Andreani, L. C.; Hu, E. L.; Petroff, P. M.; Bouwmeester, D. *Phys. Rev. Lett.* **2006**, *96*, 127404.

(34)   Sun, Q.; Wang, Y. A.; Li, L. S.; Wang, D.; Zhu, T.; Xu, J.; Yang, C.; Li, Y. *Nat. Photonics* **2007**, *1*, 717–722.

(35)   Dubertret, B.; Skourides, P.; Norris, D. J.; Noireaux, V.; Brivanlou, A. H.; Libchaber, A. *Science* **2002**, *298*, 1759–1762.

(36)   Nirmal, M.; Brus, L. *Acc. Chem. Res.* **1999**, *32*, 407–414.

(37)   Tsutsui, K.; Hu, E. L.; Wilkinson, C. D. W. *Jpn. J. Appl. Phys.* **1993**, *32*, 6233–6236.

(38)   Swihart, M. T. *Curr. Opin. Colloid Interface Sci.* **2003**, *8*, 127–133.

(39)   Maisels, A.; Kruis, F. E.; Fissan, H.; Rellinghaus, B.; Zähres, H. *Appl. Phys. Lett.* **2000**, *77*, 4431–4433.

(40) Shinde, S. R.; Kulkarni, S. D.; Banpurkar, A. G.; Nawathey-Dixit, R.; Date, S. K.; Ogale, S. B. *J. Appl. Phys.* **2000**, *88*, 1566–1575.

(41) Weber, A. P.; Seipenbusch, M.; Kasper, G. *J. Phys. Chem. A* **2001**, *105*, 8958–8963.

(42) Urban, F. K. III; Hosseini-Tehrani, A.; Griffiths, P.; Khabari, A.; Kim, Y.-W.; Petrov, I. *J. Vac. Sci. Technol. B* **2002**, *20*, 995–999.

(43) Bera, D.; Qian, L.; Tseng, T.-K.; Holloway, P. H. *Materials* **2010**, *3*, 2260–2345.

(44) La Mer, V. K.; Dinegar, R. H. *J. Am. Chem. Soc.* **1950**, *72*, 4847–4854.

(45) Murray, C. B.; Kagan, C. R.; Bawendi, M. G. *Annu. Rev. Mater. Sci.* **2000**, *30*, 545–610.

(46) Zhuang, Z.; Peng, Q.; Li, Y. *Chem. Soc. Rev.* **2011**, *40*, 5492–5513.

(47) Peng, X. G.; Manna, L.; Yang, W. D.; Wickham, J.; Scher, E.; Kadavanich, A.; Alivisatos, A. P. *Nature* **2000**, *404*, 59–61.

(48) Peng, Z. A.; Peng, X. G. *J. Am. Chem. Soc.* **2001**, *123*, 183–184.

(49) Wise, F. W. *Acc. Chem. Res.* **2000**, *33*, 773–780.

(50) Ellingson, R. J.; Beard, M. C.; Johnson, J. C.; Yu, P. R.; Micic, O. I.; Nozik, A. J.; Shabaev, A.; Efros, A. L. *Nano Lett.* **2005**, *5*, 865–871.

(51) Garcia, J. M.; Medeiros-Ribeiro, G.; Schmidt, K.; Ngo, T.; Feng, J. L.; Lorke, A.; Kotthaus, J.; Petroff, P. M. *Appl. Phys. Lett.* **1997**, *71*, 2014–2016.

(52) Marzin, J. Y.; Gerard, J. M.; Izrael, A.; Barrier, D.; Bastard, G. *Phys. Rev. Lett.* **1994**, *73*, 716–719.

(53) Gur, I.; Fromer, N. A.; Geier, M. L.; Alivisatos, A. P. *Science* **2005**, *310*, 462–465.

(54) Santra, S.; Yang, H. S.; Holloway, P. H.; Stanley, J. T.; Mericle, R. A. *J. Am. Chem. Soc.* **2005**, *127*, 1656–1657.

(55) Wang, K.; Chen, J.; Zhou, W.; Zhang, Y.; Yan, Y.; Pern, J.; Mascarenhas, A. *Adv. Mater.* **2008**, *20*, 3248–3253.

(56) Chen, N.; He, Y.; Su, Y. Y.; Li, X. M.; Huang, Q.; Wang, H. F.; Zhang, X. Z.; Tai, R. Z.; Fan, C. H. *Biomaterials* **2012**, *33*, 1238–1244.

(57) Derfus, A. M.; Chan, W. C. W.; Bhatia, S. N. *Nano Lett.* **2004**, *4*, 11–18.

(58) Stepanchikov, D. M.; Chuiko, G. P. *Condens. Matter Phys.* **2009**, *12*, 239–248.

(59) Green, M.; O'Brien, P. *Chem. Mater.* **2001**, *13*, 4500–4505.

(60) Miao, S.; Yang, T.; Hickey, S. G.; Lesnyak, V.; Rellinghaus, B.; Xu, J.; Eychmueller, A. *Small* **2013**, *9*, 3415–3422.

(61) Kimball, G. M.; Mueller, A. M.; Lewis, N. S.; Atwater, H. A. *Appl. Phys. Lett.* **2009**, *95*, 112103.

(62) Fagen, E. A. *J. Appl. Phys.* **1979**, *50*, 6505–6515.

(63) Neve, J. J.; Bouwens, C. J. R.; Blom, F. A. P. *Solid State Commun.* **1981**, *38*, 27–30.

(64) Izotov, A. D.; Sanygin, V. P.; Ponomarev, V. F. *Sov. Phys. Crystallogr.* **1978**, *23*, 429–431.

(65) Caron, L. G.; Aubin, M. J.; Jay-Gerin, J.-P. *Solid State Commun.* **1977**, *23*, 493–498.

(66) Nayak, A.; Rao, D. R. *Appl. Phys. Lett.* **1993**, *63*, 592–593.

(67) Khanna, P. K.; Singh, N.; More, P. *Curr. Appl. Phys.* **2010**, *10*, 84–88.

(68) Sharma, S. B.; Paliwal, P.; Kumar, M. *J. Phys. Chem. Solids* **1990**, *51*, 35–39.

(69)   Sierański, K.; Szatkowski, J.; Misiewicz, J. *Phys. Rev. B* **1994**, *50*, 7331–7337.

(70)   Wang, R.; Ratcliffe, C. I.; Wu, X.; Voznyy, O.; Tao, Y.; Yu, K. *J. Phys. Chem. C* **2009**, *113*, 17979–17982.

(71)   Harris, D. K.; Allen, P. M.; Han, H.-S.; Walker, B. J.; Lee, J.; Bawendi, M. G. *J. Am. Chem. Soc.* **2011**, *133*, 4676–4679.

(72)   Wyeth, N. C.; Catalano, A. *J. Appl. Phys.* **1979**, *50*, 1403–1407.

(73)   Bhushan, M.; Catalano, A. *Appl. Phys. Lett.* **1981**, *38*, 39–41.

(74)   Nayar, P. S.; Catalano, A. *Appl. Phys. Lett.* **1981**, *39*, 105–107.

(75)   Yang, R.; Chueh, Y. L.; Morber, J. R.; Snyder, R.; Chou, L. J.; Wang, Z. L. *Nano Lett.* **2007**, *7*, 269–275.

(76)   Kishore, M.; Varadaraju, U. V. *J. Power Sources* **2005**, *144*, 204–207.

(77)   Wu, P.; Dai, Y.; Ye, Y.; Yin, Y.; Dai, L. *J. Mater. Chem.* **2011**, *21*, 2563–2567.

(78)   Luber, E. J.; Mobarok, M. H.; Buriak, J. M. *ACS Nano* **2013**, *7*, 8136–8146.

(79)   Fan, J. Y.; Chu, P. K. *Small* **2010**, *6*, 2080–2098.

(80)   Li, X.; He, Y.; Talukdar, S. S.; Swihart, M. T. *Langmuir* **2003**, *19*, 8490–8496.

(81)   Hessel, C. M.; Reid, D.; Panthani, M. G.; Rasch, M. R.; Goodfellow, B. W.; Wei, J.; Fujii, H.; Akhavan, V.; Korgel, B. A. *Chem. Mater.* **2011**, *24*, 393–401.

(82)   Ruddy, D. A.; Johnson, J. C.; Smith, E. R.; Neale, N. R. *ACS nano* **2010**, *4*, 7459–7466.

(83)   Ganguly, S.; Kazem, N.; Carter, D.; Kauzlarich, S. M. *J. Am. Chem. Soc.* **2014**, *136*, 1296–1299.

(84)   Cullity, B. D. Elements of X-Ray Diffraction. *Addison-Wesley Pub. Co.* **1956**.

(85)   West, A. R. Basic Solid State Chemistry. **August 200**, *2nd Edition*.

(86)   Borchert, H.; Shevehenko, E. V.; Robert, A.; Mekis, I.; Kornowski, A.; Grubel, G.; Weller, H. *Langmuir* **2005**, *21*, 1931–1936.

(87)   Tsuge, A.; Uwamino, Y.; Ishizuka, T.; Suzuki, K. *Appl. Spectrosc.* **1991**, *45*, 1377–1380.

(88)   Nowak, M.; Kauch, B.; Szperlich, P. *Rev. Sci. Instrum.* **2009**, *80*, 046107.

(89)   Agostini, G., Lamberti, C. Characterization of Semiconductor Heterostructures and Nanostructures; *Elsevier*, **2011**.

(90)   Zaera, F. *Chem. Soc. Rev.* **2014**, *43*, 7624–7663.

(91)   Sun, T.; Wu, P. C.; Guo, Z. D.; Dai, Y.; Meng, H.; Fang, X. L.; Shi, Z. J.; Dai, L.; Qin, G. G. *Phys. Lett. A* **2011**, *375*, 2118–2121.

(92)   Fuke, S.; Imai, T.; Kawasaki, K.; Kuwahara, K. *J. Appl. Phys.* **1989**, *65*, 564–566.

(93)   Suda, T.; Kakishita, K. *J. Appl. Phys.* **1992**, *71*, 3039–3041.

(94)   Bosco, J. P.; Kimball, G. M.; Lewis, N. S.; Atwater, H. A. *J. Cryst. Growth* **2013**, *363*, 205–210.

(95)   Weber, A.; Sutter, P.; Vonkanel, H. *J. Appl. Phys.* **1994**, *75*, 7448–7455.

(96)   Lousa, A.; Bertran, E.; Varela, M.; Morenza, J. L. *Sol. Energy Mater. Sol. Cells* **1985**, *12*, 51–56.

(97)   Sathyamoorthy, R.; Sharmila, C.; Sudhagar, P.; Chandramohan, S.; Velumani, S. *Mater. Charact.* **2007**, *58*, 730–734.

(98)   Soliman, M.; Kashyout, A. B.; Osman, M.; El-Gamal, M. *Renew. Energ.* **2005**, *30*, 1819–1829.

(99)   Sudhakar, S.; Nagarajan, M.; Baskar, K. *Phys. Status Solidi C* **2012**, *9*, 1636–1639.

(100) Weller, H.; Fojtik, A.; Henglein, A. *Chem. Phys. Lett.* **1985**, *117*, 485–488.

(101) Glassy, B. A.; Cossairt, B. M. *Chem. Commun.* **2015**, **DOI:** 10.1039/C4CC08068H.

(102) Mobarok, M. H.; Luber, E. J.; Bernard, G. M.; Peng, L.; Wasylishen, R. E.; Buriak, J. M. *Chem. Mater.* **2014**, *26*, 1925–1935.

(103) Lin, S. L.; Pradhan, N.; Wang, Y. J.; Peng, X. G. *Nano Lett.* **2004**, *4*, 2261–2264.

(104) Kremser, G.; Rath, T.; Kunert, B.; Edler, M.; Fritz-Popovski, G.; Resel, R.; Letofsky-Papst, I.; Grogger, W.; Trimmel, G. *J. Colloid Interface Sci.* **2012**, *369*, 154–159.

(105) Esteves, R. J. A.; Ho, M. Q.; Arachchige, I. U. *Chem. Mater.* **2015**, *27*, 1559–1568.

(106) Chen, O.; Yang, Y. A.; Wang, T.; Wu, H. M.; Niu, C. G.; Yang, J. H.; Cao, Y. C. *J. Am. Chem. Soc.* **2011**, *133*, 17504–17512.

(107) Mobarok, M. H.; Buriak, J. M. *Chem. Mater.* **2014**, *26*, 4653–4661.

(108) Aslam, M.; Schultz, E. A.; Sun, T.; Meade, T.; Dravid, V. P. *Cryst. Growth Des.* **2007**, *7*, 471–475.

(109) Futsuhara, M.; Yoshioka, K.; Takai, O. *Thin Solid Films* **1998**, *322*, 274–281.

(110) Herring, N. P.; Panchakarla, L. S.; El-Shall, M. S. *Langmuir* **2014**, *30*, 2230–2240.

(111) Wagner, C. D., Muilenberg, G. E. Handbook of X-ray Photoelectron Spectroscopy; *Perkin-Elmer*, **1979**.

(112) Aldakov, D.; Chappaz-Gillot, C.; Salazar, R.; Delaye, V.; Welsby, K. A.; Ivanova, V.; Dunstan, P. R. *J. Phys. Chem. C* **2014**, *118*, 16095–16103.

(113) Biacchi, A. J.; Vaughn, D. D.; Schaak, R. E. *J. Am. Chem. Soc.* **2013**, *135*, 11634–11644.

(114) Tauc, J.; Grigorovici, R.; Vancu, A. *Phys. Status Solidi* **1966**, *15*, 627–637.

(115) Battaglia, D.; Peng, X. *Nano Letters* **2002**, *2*, 1027–1030.

(116) Bawendi, M. G.; Carroll, P. J.; Wilson, W. L.; Brus, L. E. *J. Chem. Phys.* **1992**, *96*, 946–954.

(117) Jones, M.; Lo, S. S.; Scholes, G. D. *Proc. Natl. Acad. Sci.* **2009**, *106*, 3011–3016.

(118) Abdellah, M.; Karki, K. J.; Lenngren, N.; Zheng, K.; Pascher, T.; Yartsev, A.; Pullerits, T. *J. Phys. Chem. C* **2014**, *118*, 21682–21686.

(119) Abel, P. R.; Chockla, A. M.; Lin, Y.-M.; Holmberg, V. C.; Harris, J. T.; Korgel, B. A.; Heller, A.; Mullins, C. B. *ACS Nano* **2013**, *7*, 2249–2257.

(120) Takeoka, S.; Toshikiyo, K.; Fujii, M.; Hayashi, S.; Yamamoto, K. *Phys. Rev. B* **2000**, *61*, 15988–15992.

(121) Kuo, Y.-H.; Lee, Y. K.; Ge, Y.; Ren, S.; Roth, J. E.; Kamins, T. I.; Miller, D. A. B.; Harris, J. S. *Nature* **2005**, *437*, 1334–1336.

(122) Minnich, A. J.; Lee, H.; Wang, X. W.; Joshi, G.; Dresselhaus, M. S.; Ren, Z. F.; Chen, G.; Vashaee, D. *Phys. Rev. B* **2009**, *80*, 155327.

(123) Canham, L. T. *Appl. Phys. Lett.* **1990**, *57*, 1046–1048.

(124) Cullis, A. G.; Canham, L. T.; Calcott, P. D. J. *J. Appl. Phys.* **1997**, *82*, 909–965.

(125) Bisi, O.; Ossicini, S.; Pavesi, L. *Surf. Sci. Rep.* **2000**, *38*, 1–126.

(126) Wilcoxon, J. P.; Provencio, P. P.; Samara, G. A. *Phys. Rev. B* **2001**, *64*, 035417.

(127)   Miguez, H.; Chomski, E.; Garcia-Santamaria, F.; Ibisate, M.; John, S.; López, C.;

Meseguer, F.; Mondia, J. P.; Ozin, G. A.; Toader, O. *Adv. Mater.* **2001**, *13*, 1634–

1637.

(128)   Ruddy, D. A.; Erslev, P. T.; Habas, S. E.; Seabold, J. A.; Neale, N. R. *J. Phys.

Chem. Lett.* **2013**, *4*, 416–421.

(129)   Vaughn, D. D.; Bondi, J. F.; Schaak, R. E. *Chem. Mater.* **2010**, *22*, 6103–6108.

VITA

Minh Q. Ho

Date of birth: February 4, 1987

Place of birth: Da Nang, Vietnam

Country of citizenship: Vietnam

Email: minhqho87@gmail.com

Phone : (804) 869-8322

EDUCATION

(2010 – now)   Virginia Commonwealth University, Richmond, Virginia

- Master of Science in Chemistry

- Graduation Date: August 2015

- GPA: 3.05/4.00

- Advisor: Dr. Indika U. Arachchige

(2005–2009)   Truman State University, Kirksville, Missouri

- Bachelor of Science in Chemistry

- GPA: 3.25/4.00

AWARDS

- Outstanding Teaching Assistant Award   Virginia Commonwealth University

- President's Honorary Scholarship   Truman State University

RESEARCH EXPERIENCES

- August 2012 – July 2015

  ➢ Designed and developed colloidal synthetic method for low-toxic group II-V and IV-IV semiconducting nanomaterials.

  ➢ Optimized the synthetic conditions by tuning reaction parameters (solvent composition, reactant concentration, growth time, temperature) for phase-pure and high-quality products.

  ➢ Investigated their optical properties as a function of size, shape and composition.

- May 2011 – July 2012

  ➢ Established a microwave synthesis of Fe-based nanomaterials supported on graphene or carbon nanotubes, and evaluated their catalytic properties for production of liquid hydrocarbons from synthetic gas.

  ➢ Synthesized and examined the catalytic activities of Au and Pd supported on CeO_2/graphene or TiO_2/graphene toward the oxidation of carbon monoxide.

  ➢ Designed a Laser Vaporization Controlled Condensation (LVCC) synthesis of nitrogen- and boron-doped graphene.

- May 2010 – April 2011

  ➢ Explored the formation and polymerization mechanism of carbon cluster ions by laser ablation of graphite and graphite oxide in supersonic expansion environments.

  ➢ Identified the appropriate conditions (carrier gas, temperature, pressure, laser power) for optimized cluster polymerization.

PUBLICATIONS AND PROFESSIONAL PRESENTATIONS

Virginia Commonwealth University

- Minh Q. Ho, Richard J Alan Esteves, Gotluru Kedarnath, and Indika U. Arachchige. Size-Dependent Optical Properties of Luminescent Zn_3P_2 Quantum Dots. *J. Phys. Chem. C* **2015**, **DOI:** 10.1021/acs.jpcc.5b01747.

- Richard J Alan Esteves, Minh Q. Ho, and Indika U. Arachchige. Nanocrystalline Group IV Alloy Semiconductors: Synthesis and Characterization of $Ge_{1-x}Sn_x$ Quantum Dots for Tunable Bandgaps. *Chem. Mater.* **2015**, *27*, 1559–1568.

- Sherif O. Moussa, Leela S. Panchakarla, Minh Q. Ho, and M. Samy El-Shall. Graphene-Supported, Iron-Based Nanoparticles for Catalytic Production of Liquid Hydrocarbons from Synthesis Gas: The Role of the Graphene Support in Comparison with Carbon Nanotubes. *ACS Catal.* **2014**, *4*, 535–545.

- Minh Q. Ho and Indika U. Arachchige. Colloidal Synthesis of Group IV and II-V Semiconducting Nanocrystals. *Virginia Commonwealth University Poster Presentation*. **2013**.

- Minh Q. Ho and M. Samy El-Shall. Organic Donor-Acceptor Bulk Heterojunction (DABHJ) Solar Cells and the Future of Solar Energy Conversion. *Virginia Commonwealth University Literature Seminar*. **2011**.

- Minh Q. Ho, Sherif Moussa and M. Samy El-Shall. Synthesis and Characterization of Graphene Sheets by Rapid Thermal Expansion of Graphite Oxide Pellets. *Virginia Commonwealth University Poster Presentation*. **2011**.

- Minh Q. Ho, Isaac K. Attah and M Samy El-Shall. Generation of Carbon Cluster Ions from Graphite and Graphite Oxide Using Laser Vaporization/Ionization. *Virginia Commonwealth University Poster Presentation*. **2010**.

Truman State University

- Minh Q. Ho, Emery Brown, Richard Knopik, Patrick Kilgore, Brian Lamp and David McCurdy. Determination of Mercury in Freshwater Fish Using Cold Vapor Atomic Absorption Spectrophotometry (CV-AAS)*. Truman State University Merck/AAAS Oral Presentation*. **2009**.

- Minh Q. Ho, Emery Brown, Richard Knopik, Patrick Kilgore, Brian Lamp and David McCurdy. Atomic Absorption Determination of Mercury in Local Freshwater Fish Using a Home-Built Cold Vapor Generator*. ACS Regional Oral Presentation*. **2009**.

TEACHING EXPERIENCES

Virginia Commonwealth University: *Graduate Teaching Assistant* (Jan 2010 – present)

- Conducted general chemistry laboratory classes (CHEZ 101 & 102). Guided students in completing lab experiments; evaluated and helped them gain better understanding about the chemistry involved.

- Assisted the professor in coordinating and teaching students in Instrument Analysis laboratory (CHEZ 409). Prepared chemicals and helped designing laboratory experiments that are more applicable for students. Aided students in understanding how instrumental laboratory experiments can be utilized in many real-life applications.

Truman State University: *Math Tutor* (Aug 2007 – May 2009)

- Aided students in completing their math assignments in pre-calculus, algebra, geometry, trigonometry, calculus I, and reviewing what they have learned in class to prepare for exams.

- Help them reviewing materials learned in class to prepare for examinations.